Shortwave radiative forcing, rapid adjustment, and feedback to the surface by sulphate geoengineering: Analysis of the Geoengineering Model Intercomparison Project G4 scenario

Hiroki Kashimura[1,a], Manabu Abe[1], Shingo Watanabe[1], Takashi Sekiya[1], Duoying Ji[2], John C. Moore[2], Jason N. S. Cole[3], and Ben Kravitz[4]

[1]Japan Agency for Marine-Earth Science and Technology, Yokohama, Japan.
[2]College of Global Change and Earth System Science, Beijing Normal University, Beijing, China.
[3]Canadian Centre for Climate Modelling and Analysis, Environment and Climate Change Canada, Victoria, British Columbia, Canada.
[4]Atmospheric Sciences and Global Change Division, Pacific Northwest National Laboratory, Washington, USA.
[a]current affiliation: Department of Planetology/Center for Planetary Science, Kobe University, Kobe, Japan.

Correspondence to: Hiroki Kashimura (hiroki@cps-jp.org)

Abstract. This study evaluates the forcing, rapid adjustment, and feedback of net shortwave radiation at the surface in the G4 experiment of the Geoengineering Model Intercomparison Project by analysing outputs from six participating models. G4 involves injection of $5 \, \mathrm{Tg \, yr^{-1}}$ of SO_2, a sulphate aerosol precursor, into the lower stratosphere from year 2020 to 2070 against a background scenario of RCP4.5. A single layer atmospheric model for shortwave radiative transfer is used to estimate the direct forcing of solar radiation management (SRM), and rapid adjustment and feedbacks from changes in the water vapour amount, cloud amount, and surface albedo (compared with RCP4.5). The analysis shows that the globally and temporally averaged SRM forcing ranges from -3.6 to $-1.6 \, \mathrm{W \, m^{-2}}$, depending on the model. The sum of the rapid adjustments and feedback effects due to changes in the water vapour and cloud amounts increase the downwelling shortwave radiation at the surface by approximately 0.4 to $1.5 \, \mathrm{W \, m^{-2}}$ and hence weaken the effect of SRM by around 50 %. The surface albedo changes decrease the net shortwave radiation at the surface; it is locally strong ($\sim -4 \, \mathrm{W \, m^{-2}}$) in snow and sea ice melting regions, but minor for the global average. The analyses show that the results of the G4 experiment, which simulates sulphate geoengineering, include large inter-model variability both in the direct SRM forcing and the shortwave rapid adjustment from change in the cloud amount, and imply a high uncertainty in modelled processes of sulphate aerosols and clouds.

1   Introduction

Geoengineering, or climate engineering, is the deliberate large-scale manipulation of the planetary environment to counteract anthropogenic climate change (e.g., Shepherd, 2009). One major category of geoengineering for lessening the effects of global warming is solar radiation management (SRM), which aims to reduce the amount of solar radiation at the Earth's surface. One of several SRM approaches (e.g., Lane et al., 2007) is to mimic a volcanic eruption by injecting sulphate aerosol precursors, such as SO_2, into the stratosphere (e.g., Budyko, 1974; Crutzen, 2006); this approach is called sulphate geoengineering. Large

volcanic eruptions carry SO_2 gases into the stratosphere; these gases are photo-chemically oxidized to form sulphate aerosols, which have high reflectivity in the visible and ultraviolet regions of the electromagnetic spectrum. Sulphate aerosols increase the solar reflectivity of the atmosphere, decreasing the shortwave radiation (SW) reaching the surface, and therefore cooling the air temperature. For example, the 1991 eruption of Mount Pinatubo reduced the globally averaged surface air temperature by up to 0.5 K (Parker et al., 1996).

To explore the cooling effect of and the climate responses from sulphate geoengineering, or more generally SRM, several climate-modelling groups performed various experiments using global climate models or Earth System Models (ESMs). Some experiments involved simplifying the net effects of SRM by reducing the solar constant. Govindasamy and Caldeira (2000) and Bala et al. (2008) performed a CO_2 doubling experiment with a 1.8 % reduction of the solar constant, and showed that such a decrease would compensate the global mean temperature change caused by the CO_2 doubling in their models. Govindasamy et al. (2002) considered the impact of the solar constant reduction on the terrestrial biosphere, whilst a CO_2 quadrupling experiment with a 3.6 % reduction of the solar constant was explored in Govindasamy et al. (2003). Furthermore, Matthews and Caldeira (2007) adopted the IPCC A2 scenario (IPCC, 2007) as their reference simulation and performed experiments in which the geoengineering was applied for different years. Others have simulated sulphate geoengineering with models that can partly or fully calculate the production of sulphate aerosols from the injected SO_2 and the dynamical transportation. For example, Rasch et al. (2008a) designed their experiments with SO_2 injection by 2–4 $Tg\,yr^{-1}$ in an equatorial region with doubled CO_2, whereas Robock et al. (2008) adopted the A1B scenario as their baseline run and injected 3–10 $Tg\,yr^{-1}$ of SO_2 from arctic or tropical regions in their simulation. The models used in these two studies include formation, transportation, and removal of the stratospheric sulphate aerosols, but the particle size distribution was prescribed. Heckendorn et al. (2009) and Pierce et al. (2010) calculated full microphysics of sulphate aerosols with an assumption of zonally homogeneous conditions. They simulated 2–20 $Tg\,yr^{-1}$ SO_2 injection with a present day (year 2000) condition run as their reference simulation. Niemeier and Timmreck (2015) used models with full microphysics of sulphate aerosols, and performed a sulphate geoengineering experiment with SO_2 injection rates of 2–200 $Tg\,yr^{-1}$ to counteract the anthropogenic forcing of RCP8.5. Most of the aforementioned studies used different forcing and/or schemes for geoengineering, different scenarios for the baseline, and different models. Therefore, it is difficult to compare these studies or evaluate the uncertainty in the geoengineering simulations. However, Jones et al. (2010) compared the results of two different models in an experiment similar to that of Robock et al. (2008). They showed the different responses by the two models and emphasized the importance of intercomparing many different climate models with a common experimental design in order to assess the impact of the geoengineering.

The Geoengineering Model Intercomparison Project (GeoMIP) (Kravitz et al., 2011) was established to coordinate simulations with a common framework and to determine the robust effects and responses to geoengineering processes. For the first series of GeoMIP experiments, four experiments named G1, G2, G3, and G4 were proposed. The first two are designed to counteract quadrupled CO_2 radiative forcing (G1) and a 1 % increase in the CO_2 concentration per year (G2) by simply reducing the solar constant. The last two are designed to inject SO_2 into the lower stratosphere and decrease SW flux reaching the surface by increasing the SW reflection by sulphate aerosols. Both G3 and G4 use the RCP4.5 scenario for the baseline experiment and inject SO_2 every year from 2020 to 2070. The amount of SO_2 injected in G3 gradually increases

to maintain the net radiative flux at the top-of-atmosphere (TOA) at the 2020 levels, while the radiative forcing of the greenhouse gases increases according to the RCP4.5 scenario. Conversely, in G4 the SO_2 injection rate is fixed at 5 $Tg\,yr^{-1}$. A summary of the G1–G4 studies is presented by Kravitz et al. (2013d) and the latest list of GeoMIP studies is available at http://climate.envsci.rutgers.edu/GeoMIP/index.html.

5   As summarized by Kravitz et al. (2013d), studies analysing GeoMIP experiments have explored and clarified climate model responses to radiative forcing and its dependence on various factors. In addition, the dependence (or uncertainty) of the direct forcing to the net surface SW induced by sulphate aerosol injection (hereafter SRM forcing) on models should be also studied well, since estimation of the SRM forcing is important when considering the costs and benefits of geoengineering. The G1 and G2 experimental designs have limited utility in understanding sulphate aerosol geoengineering because the SRM is introduced

10   simply and directly by the reduction of the solar constant. In G3, the amount of injected SO_2 mimicked in each model varies by year, which is useful for controlling the absolute amount of forcing but not the injection rate. In contrast, in G4 the rate of SO_2 injection is fixed at 5 $Tg\,yr^{-1}$ throughout the SRM period, and the annually averaged strength of the SRM forcing should be almost constant during the SRM period in each model, but may differ among models. Therefore, the G4 experiment is suitable for directly exploring the strength and the model dependence or uncertainty of the SRM forcing.

15   There are numerous sources of inter-model differences in response to the same (or similar) forcing. On processes related to the SRM forcing, modelled aerosol microphysics including formation, growth, transportation, and removal may differ, and such differences result in the difference in meridional distribution of the aerosol optical depth (AOD). Even though the prescribed AOD is given, a difference in an assumed particle size for the stratospheric sulphate aerosols causes difference in the SRM forcing (Pierce et al., 2010). On a broad scale, different models have distinct climate sensitivities and thus different global mean

20   temperature responses to the same forcing. In addition, different models have various representations of processes, which affects the direct response to the forcing as well as different feedback from the responses. For example, cloud adjustments (Schmidt et al., 2012), sea ice changes (Moore et al., 2014), and stratospheric ozone changes (Pitari et al., 2014) are all known to affect the climate response to geoengineering through feedback. The ocean response operates on longer timescales and has also been shown to be important in understanding the response to geoengineering (Kravitz et al., 2013b). Yu et al.

25   (2015) calculated the difference in globally and temporally averaged near-surface air temperature of G4 (over 2030–2069) from "baseline climate" (RCP4.5 over 2010–2029) and showed a standard deviation of up to ±0.31 K among models, while the model mean of the temperature difference was 0.28 K. Whilst the models in G4 assume the same rate of SO_2 injection, model responses to the SRM differ widely. Investigation into what causes such a large inter-model variability is very important for SRM simulation studies.

30   A simple procedure is used for quantifying the contributions of different types of SW rapid adjustments and feedbacks in the climate model behaviour to geoengineering with stratospheric sulphate aerosols. Here, a rapid adjustment is defined as a reaction to the SRM forcing without changes in globally averaged surface air temperature, whereas a feedback is defined as a reaction due to surface air temperature changes in the global mean induced by the SRM forcing (e.g., Sherwood et al., 2015). (Hereafter, the term "total reaction" refers to the sum of a rapid adjustment and a feedback.) In recent studies of the climate

35   change, rapid adjustments are included in forcing agents and the concept of effective radiative forcing is widely used. However,

for the study of the sulphate geoengineering simulation, which is not well verified by observations and thus is expected to have many uncertainties, the separation of the direct forcing and total reactions is important to improve the simulation and to enhance the degree of understanding of the sulphate geoengineering by refining individual related processes. Many studies on climate energy balance have analysed changes in the net radiation flux at TOA, where the energy budget is closed by SW

5   and longwave radiation (LW). However, in the geoengineering study, the radiative changes at the surface are also important, because vegetation, agriculture, and solar power generation for example will be strongly affected by radiative changes at the surface as well as surface temperature changes. Though the surface energy budget is balanced among SW, LW, sensible heat flux, and latent heat flux, Kleidon et al. (2015) showed that the latter three are mainly determined by the air and/or surface temperature. Hence, this study focuses on changes in surface air temperature and SW. The direct SW forcing to the surface are

10   evaluated by considering the total reactions due to changes in water vapour amounts, cloud amounts, and surface albedo. Also, these total reactions are decomposed into adjustments and feedbacks, which indicate the rapid change just after injection of SO_2 and the change with globally averaged surface air temperature change by SRM, respectively. We provide results for both global and local effects, focusing on cross-model commonalities and differences. The following section describes the data and methods used in this study. Section 3 presents the results of the analyses. Section 4 provides a short discussion. Summary and

15   concluding remarks are provided in Section 5.

2   Data and methods

The models analysed in this study are listed in Table 1. Note that the method of simulating sulphate aerosols differs among the participating models. HadGEM2-ES and MIROC-ESM-CHEM-AMP calculate the formation of sulphate aerosols from SO_2 injected from the lower stratosphere on the equator, and their horizontal distribution of sulphate AODs differ. BNU-

20   ESM, MIROC-ESM, and MIROC-ESM-CHEM use a prescribed AOD, which is formulated as one fourth of the strength of the 1991 eruption of Mount Pinatubo following Sato et al. (1993) and provided in http://climate.envsci.rutgers.edu/GeoMIP/ geomipaod.html. The annual cycle and latitudinal distribution of the prescribed AOD, which is zonally uniform, is shown in Fig. 1; this annual cycle is repeated every year during the SRM period. In CanESM2, a constant field of AOD (~ 0.047) has been given to express the effect of the SO_2 injection. The MIROC-ESM, MIROC-ESM-CHEM, and MIROC-ESM-CHEM-

25   AMP are based on the same framework but differ in their treatment of atmospheric chemistry. An online atmospheric chemistry module is coupled in the MIROC-ESM-CHEM and MIROC-ESM-CHEM-AMP, whereas MIROC-ESM is not coupled with the chemistry module. In the MIROC-ESM-CHEM, the prescribed AOD is used for the stratospheric sulphate aerosols and for the calculation of the surface area density of the sulphur. Conversely, the MIROC-ESM-CHEM-AMP fully calculates the chemistry and micro-physics of the stratospheric sulphate aerosol formation from SO_2 (a detailed description is presented in

30   Sekiya et al., 2016).

The mean stratospheric sulphate aerosol particle sizes and standard deviation of their log-normal distribution (σ) in each model are shown in Table 1. In HadGEM2-ES, the tropospheric aerosol scheme and the associated microphysical properties (Bellouin et al., 2011) is simply extended into the stratosphere. Modifications to the stratospheric aerosol size distribution have

been applied in subsequent HadGEM2-ES studies (Jones et al., 2016a, b), but have not been applied here. In MIROC-ESM-CHEM-AMP, the microphysics module for stratospheric sulphate aerosols treats them in three modes as shown in Table 2 in Sekiya et al. (2016); however, to calculate radiative processes on the aerosols, a particle size of 0.243 μm is assumed for simplification. In addition, the microphysics of the tropospheric sulphate aerosols is not calculated in MIROC-ESM-CHEM-AMP to avoid drift in the simulated climate.

Note that the following four models also participated in the GeoMIP-G4 experiment but are not used in this study. CSIRO Mk3L (Phipps et al., 2011, 2012) mimics the effect of SO_2 injection by reduction of the solar constant, so the method of analysis described below cannot be used. GEOSCCM (Rienecker et al., 2008) and ULAQ (Pitari et al., 2002) do not include an ocean model and the sea surface temperature is prescribed, so that the surface temperature decrease by the SRM is not simulated in a way that is conducive to the analyses undertaken. GISS-E2-R (Schmidt et al., 2006) has issues in its output of clear-sky SW flux at the surface that preclude the incorporation of this data in the analyses.

The model output variables used in this study are monthly means of surface air temperature (T), upwelling and downwelling SW fluxes at the surface and TOA for all-sky and clear-sky. The data for both experiments (RCP4.5 and G4) from the models listed in Table 1 with all ensemble members are used.

Since the SRM forcing is mainly induced by the reflection of the SW by stratospheric sulphate aerosols, the atmospheric reflection rate is very important. In order to consider rapid adjustments and feedbacks on the SW due to the SRM forcing, the atmospheric absorption rate and the surface albedo are also important. To estimate these rates and the albedo from SW fluxes described in the previous paragraph, a single-layer atmospheric model of SW transfer used in Donohoe and Battisti (2011) (hereafter DB11) is applied. DB11's single-layer model assumes that a fraction R of the downwelling solar radiation flux at the TOA S is reflected back to space, and a fraction A is absorbed by the atmosphere at the same single layer. A fraction α of the transmitted radiation flux $S(1 - R - A)$ is then reflected by the surface. This reflected upwelling radiative flux is reflected back to the surface at the rate of R and absorbed at the rate of A at the atmospheric layer, and the remainder $S\alpha(1 - R - A)^2$ is transmitted to space. This process continues, forming an infinite geometric series, as shown in Fig. 1 of DB11; therefore, the TOA upwelling SW flux ($F_{\text{TOA}}^{\uparrow}$), surface downwelling SW flux ($F_{\text{SURF}}^{\downarrow}$), and surface upwelling SW flux ($F_{\text{SURF}}^{\uparrow}$) can be written as follows:

$$
\begin{aligned}
F_{\text{TOA}}^{\uparrow} &= S\left[R + \alpha(1 - R - A)^2 + \alpha^2 R(1 - R - A)^2 + \alpha^3 R^2(1 - R - A)^2 + \cdots\right] \\
&= SR + \alpha S(1 - R - A)^2\left[1 + (\alpha R) + (\alpha R)^2 + \cdots\right] = SR + \alpha S\frac{(1 - R - A)^2}{1 - \alpha R},
\end{aligned}
\tag{1}
$$

$$
\begin{aligned}
F_{\text{SURF}}^{\downarrow} &= S\left[(1 - R - A) + \alpha R(1 - R - A) + \alpha^2 R^2(1 - R - A) + \alpha^3 R^3(1 - R - A) + \cdots\right] \\
&= S(1 - R - A)\left[1 + (\alpha R) + (\alpha R)^2 + (\alpha R)^3 + \cdots\right] = S\frac{(1 - R - A)}{1 - \alpha R},
\end{aligned}
\tag{2}
$$

$$
F_{\text{SURF}}^{\uparrow} = \alpha F_{\text{SURF}}^{\downarrow} = \alpha S\frac{(1 - R - A)}{1 - \alpha R}.
\tag{3}
$$

Here, the infinite series in the second lines of Eqs. (1) and (2) converge to the final expression on the right-hand side because $\alpha R < 1$. The fractions R, A, and α are positive and less than unity. Note that, to the best of our knowledge, the idea of forming

the infinite geometric series from SW transfer between a single layer and the surface can be traced back to Rasool and Schneider (1971), who calculated the effect of aerosol on the global temperature by considering a single aerosol layer.

From Eqs. (1)–(3), R, A, and α can be calculated when S, $F_{\text{TOA}}^{\uparrow}$, $F_{\text{SURF}}^{\downarrow}$, and $F_{\text{SURF}}^{\uparrow}$ are given. Surface albedo α can be obtain immediately by Eq. (3) as

$$\alpha = \frac{F_{\text{SURF}}^{\uparrow}}{F_{\text{SURF}}^{\downarrow}}. \tag{4}$$

5 Substitution of the product of Eqs. (2) and (3) into Eq. (1) yields

$$R = \frac{S F_{\text{TOA}}^{\uparrow} - F_{\text{SURF}}^{\downarrow} F_{\text{SURF}}^{\uparrow}}{S^2 - F_{\text{SURF}}^{\uparrow 2}}, \tag{5}$$

for calculating the value of R. Then, A is calculated using values of R and α by the following form of Eq. (2):

$$A = (1 - R) - \frac{F_{\text{SURF}}^{\downarrow}}{S}(1 - \alpha R). \tag{6}$$

Note that, R, A, and α cannot be obtained when $S = 0$ such as during the polar night.

Based on the DB11's single-layer model described above, the strength of the SRM forcing and the total reactions due to changes in the water vapour amount, cloud amount, and surface albedo are estimated using the method described in the

10 remainder of this section. Since GeoMIP participating models provide all-sky and clear-sky values for $F_{\text{TOA}}^{\uparrow}$, $F_{\text{SURF}}^{\downarrow}$, and $F_{\text{SURF}}^{\uparrow}$, values of R, A, and α can be calculated for both all-sky and clear-sky; superscript "as" is used for all-sky and "cs" for clear-sky. Defining the cloud effects on a variable X by $X^{\text{cl}} \equiv X^{\text{as}} - X^{\text{cs}}$, the all-sky value is the sum of the clear-sky value and the cloud effect: $X^{\text{as}} = X^{\text{cs}} + X^{\text{cl}}$, where superscript "cl" is for the cloud effect. For further simplicity, the cloud effect on the surface albedo is assumed to be negligible (i.e., $\alpha^{\text{as}} \approx \alpha^{\text{cs}}$), and α^{as} is used in the following analyses and the superscript

15 omitted. Now, the monthly mean of R^{cs}, R^{cl}, A^{cs}, A^{cl}, and α is calculated on each grid-point for RCP4.5 and G4 experiments.

Net SW at the surface is a key variable in this study and can be written as follows:

$$F_{\text{SURF}}^{\text{net}} \equiv F_{\text{SURF}}^{\downarrow \text{as}} - F_{\text{SURF}}^{\uparrow \text{as}} = (1 - \alpha) S \left[\frac{1 - (R^{\text{cs}} + R^{\text{cl}}) - (A^{\text{cs}} + A^{\text{cl}})}{1 - \alpha(R^{\text{cs}} + R^{\text{cl}})} \right]. \tag{7}$$

Here, $F_{\text{SURF}}^{\text{net}}$ is regarded as a function of S, R^{cs}, R^{cl}, A^{cs}, A^{cl}, and α. The difference of $F_{\text{SURF}}^{\text{net}}$ between RCP4.5 and G4 experiments is defined as

$$\Delta F_{\text{SURF}}^{\text{net}} \equiv F_{\text{SURF}}^{\text{net}}(S, R_{\text{G4}}^{\text{cs}}, R_{\text{G4}}^{\text{cl}}, A_{\text{G4}}^{\text{cs}}, A_{\text{G4}}^{\text{cl}}, \alpha_{\text{G4}}) - F_{\text{SURF}}^{\text{net}}(S, R_{\text{RCP}}^{\text{cs}}, R_{\text{RCP}}^{\text{cl}}, A_{\text{RCP}}^{\text{cs}}, A_{\text{RCP}}^{\text{cl}}, \alpha_{\text{RCP}}), \tag{8}$$

where the experiment names are indicated by subscripts "RCP" and "G4". (S, the TOA downwelling solar radiation, is same

20 for RCP4.5 and G4.) Hereafter, $F_{\text{SURF}}^{\text{net}}(\text{RCP}) \equiv F_{\text{SURF}}^{\text{net}}(S, R_{\text{RCP}}^{\text{cs}}, R_{\text{RCP}}^{\text{cl}}, A_{\text{RCP}}^{\text{cs}}, A_{\text{RCP}}^{\text{cl}}, \alpha_{\text{RCP}})$ is written for convenience.

To estimate the strength of the SRM forcing and the total reactions due to changes in the water vapour amount, cloud amount, and surface albedo on the net SW at the surface, the following is assumed:

1. The sulphate aerosols increased by the SO_2 injection amplify the reflection rate of the clear-sky atmosphere (R^{cs}), whilst their effect on the absorption rate (A^{cs}) is negligible.

2. The change in water vapour amount affects the absorption rate of the clear-sky atmosphere (A^{cs}), whilst its effect on the reflection rate (R^{cs}) is negligible.

3. The amounts of other substances that affects the reflection or absorption rate of the clear-sky atmosphere do not change considerably, and their effects are negligible.

5 Though the sulphate aerosols can absorb near infrared radiation, which is a part of SW, its effect on the SRM forcing is ignored since its amount is insignificant compared to the SW reflected by the sulphate aerosols (Haywood and Ramaswamy, 1998). (An error due to ignoring the SW absorption by the sulphate aerosols is estimated at the end of this paper.)

Under the above assumptions, the strength of the SRM forcing F_{SRM} is defined by

$$F_{SRM} \equiv F_{SURF}^{net}(S, R_{G4}^{cs}, R_{RCP}^{cl}, A_{RCP}^{cs}, A_{RCP}^{cl}, \alpha_{RCP}) - F_{SURF}^{net}(RCP). \tag{9}$$

This is a change of net surface SW when only R^{cs} is changed to the value of G4. Similarly, the effects of total reactions from
10 changes in the water vapour amount (E_{WV}), cloud amount (E_C), and surface albedo (E_{SA}) are defined as follows:

$$E_{WV} \equiv F_{SURF}^{net}(S, R_{RCP}^{cs}, R_{RCP}^{cl}, A_{G4}^{cs}, A_{RCP}^{cl}, \alpha_{RCP}) - F_{SURF}^{net}(RCP), \tag{10}$$

$$E_C \equiv F_{SURF}^{net}(S, R_{RCP}^{cs}, R_{G4}^{cl}, A_{RCP}^{cs}, A_{G4}^{cl}, \alpha_{RCP}) - F_{SURF}^{net}(RCP), \tag{11}$$

$$E_{SA} \equiv F_{SURF}^{net}(S, R_{RCP}^{cs}, R_{RCP}^{cl}, A_{RCP}^{cs}, A_{RCP}^{cl}, \alpha_{G4}) - F_{SURF}^{net}(RCP). \tag{12}$$

Here, the following three points should be noted. First, E_{WV}, E_C, and E_{SA} are measures for the sum of SW radiative rapid adjustment and feedback, and do not include any LW effects; changes in the water vapour and cloud amounts can, however, affect LW transfer. Second, the sum of F_{SRM}, E_{WV}, E_C, and E_{SA} is not exactly equal to ΔF_{SURF}^{net}, since Eq. (7) is not linear. However, if $\Delta F_{SURF}^{net} \approx F_{SRM} + E_{WV} + E_C + E_{SA}$ is satisfied, it can be stated that the decomposition of ΔF_{SURF}^{net} into F_{SRM}, E_{WV},
15 E_C, and E_{SA} is reasonable. Finally, E_C includes both the effect of changes in cloud cover and cloud albedo. This is because R^{cl} and A^{cl} can be written as follows, by expressing R^{as} and A^{as} with the total cloud-area fraction γ, the reflection rate of a fully cloud-covered atmosphere r^{fca}, and the absorption rate of a fully cloud-covered atmosphere a^{fca},

$$R^{cl} = R^{as} - R^{cs} = (1 - \gamma)R^{cs} + \gamma r^{fca} - R^{cs} = \gamma(r^{fca} - R^{cs}), \tag{13}$$

$$A^{cl} = A^{as} - A^{cs} = (1 - \gamma)A^{cs} + \gamma a^{fca} - A^{cs} = \gamma(a^{fca} - A^{cs}). \tag{14}$$

These expressions mean that cloud effects (R^{cl} and A^{cl}) include both the total cloud-area fraction and reflection or absorption rate of a fully cloud-covered atmosphere, which depends on cloud albedo or absorption rate. Therefore, E_C includes both the
20 effect of changes in coverage, albedo and SW absorption rate of clouds. In addition, E_C should not include the "masking effect" (Zhang et al., 1994; Colman, 2003; Soden et al., 2004) of the clouds because the clear-sky values R^{cs} and A^{cs} are unchanged from those in RCP4.5.

In this study, the SRM forcing and the three total reactions on net SW at the surface from the changes in the water vapour amount, cloud amount, and surface albedo, defined by Eqs. (9)–(12), are calculated on each grid-point where $S > 0$ from the
25 monthly mean data. At grid points where $S = 0$, $F_{SRM} = E_{WV} = E_C = E_{SA} = 0$.

To decompose the total reactions (E_{WV}, E_C, and E_{SA}) into rapid adjustments and feedbacks, a method similar to the Gregory plot (Gregory et al., 2004) is used. That is, the globally and annually averaged data of total reactions are plotted against that of ΔT ($\equiv T_{G4} - T_{RCP}$), and linear regression lines in the following forms are obtained by the least squares method.

$$\overline{E_{WV}} = Q_{WV} - P_{WV}\overline{\Delta T}, \tag{15}$$

$$\overline{E_C} = Q_C - P_C\overline{\Delta T}, \tag{16}$$

$$\overline{E_{SA}} = Q_{SA} - P_{SA}\overline{\Delta T}. \tag{17}$$

Here, Q_X ($X =$ WV, C, SA) denotes the rapid adjustment, $-P_X$ is the feedback parameter, and the overline denotes the global and annual average. This method is similar to the Gregory plot, but note that ΔT is the surface temperature difference between the G4 experiment and the RCP4.5 scenario experiment in which the anthropogenic radiative forcing depends on time and the simulated climate does not reach an statistically equilibrium state.

3 Results

3.1 Surface air temperature and shortwave radiation

Figure 2 shows the time series of globally averaged surface air temperature (T) with a 12-month running mean for G4 (solid) and RCP4.5 (dashed). For all models, T in G4 decreases or remains at the 2020 level for a few decades and begins increasing from around 2040 or earlier, whereas T in RCP4.5 steadily increases. Accordingly, the difference in T between RCP4.5 and G4 increases for 10–25 years from 2020 and then stops rising. That is, the cooling effect of SRM gradually affects the global mean of T because of slow feedback and/or thermal inertia of the modelled climate system, and takes a few decades to reach steady state. After that, the SRM becomes unable to prevent the temperature from increasing any more, delaying global warming for a few decades as compared with RCP4.5. In addition, after halting SRM at 2070, T increases rapidly and then returns to the RCP4.5 level in each model. This rapid increase has been called the termination effect of SRM (e.g., Wigley, 2006; Jones et al., 2013; Kravitz et al., 2013d).

To properly compare the SRM effects among the models, we eliminate some of the transient behaviour and focus on the years 2040 to 2069, in which the amount of cooling in G4 compared with RCP4.5 is roughly kept constant. (Although the reason for the transient behaviour of the SRM's cooling effect is an important topic, it is beyond the scope of this study.) Figure 3 shows the relationship between ΔT and ΔF_{SURF}^{net}, the difference in net SW at the surface, averaged over the globe, for 2040–2069. For CanESM2, HadGEM2-ES, and MIROC-ESM-CHEM, the filled symbols indicate the ensemble mean whilst the unfilled symbols indicate individual ensemble members; for the other models, the filled symbols indicate the results of a single run. This figure shows a strong correlation between the mean ΔT and ΔF_{SURF}^{net}; the correlation coefficient for the six filled symbols is 0.88. This strong correlation allows ΔF_{SURF}^{net} to be used as a measure of the SRM effects at least for $-1.1 \lesssim \Delta T \lesssim -0.2$ K, although the surface air temperature depends on the energy balance among SW, LW, and sensible and latent heat fluxes at the surface. Moreover, as described at the end of Section 1, it is important to explore the SW flux at the surface to estimate the effect

of SRM on vegetation and human activities such as agriculture and solar power generation. Therefore, this study mainly focuses on SW at the surface and estimates the SRM forcing and total reactions of SW due to changes in the water vapour amount, cloud amount, and surface albedo. One concern is that half the models used in this study have only one ensemble member, and half are MIROC-based models. The effects of this are analysed in Section 4.3 and shown to be relatively unimportant.

3.2 Time-evolution of global mean forcing and SW total reactions

The strength of the SRM forcing (F_{SRM}) defined by Eq. (9) and the SW total reactions due to changes in the water vapour amount (E_{WV}), cloud amount (E_{C}), and surface albedo (E_{SA}) defined by Eqs. (10)–(12) are calculated for each model. Figure 4 shows the time-evolution of the globally averaged values of these measures with a 12-month running mean. $\Delta F_{\mathrm{SURF}}^{\mathrm{net}}$ and ΔT are also shown in this figure. In this subsection, the focus is on the qualitative features common to all or some of the models, whilst the quantitative differences are described in the following subsection.

In the models that used the prescribed or constant AOD field for the SRM (BNU-ESM, CanESM2, MIROC-ESM, and MIROC-ESM-CHEM), F_{SRM} (red) immediately reaches a model-dependent negative value after 2020 and remains almost constant; it then vanishes instantly after the termination. These features are consistent with the fact that the given AOD for the SRM was instantly added and removed in these models. Conversely, in the models that calculate the formation and transport of the sulphate aerosols from the injected SO_2 (HadGEM2-ES and MIROC-ESM-CHEM-AMP), F_{SRM} takes approximately four years to become saturated. During the period in which SRM is imposed, F_{SRM} in MIROC-ESM-CHEM-AMP is almost constant, but F_{SRM} in HadGEM2-ES varies by approximately $1.0\ \mathrm{W\,m^{-2}}$.

The values of E_{SA} shown by the green curves are both negative and small in all of the models. This shows that, at least for the global average, the surface albedo under G4 is higher than that under RCP4.5. However, changes in the surface albedo do not significantly affect $\Delta F_{\mathrm{SURF}}^{\mathrm{net}}$.

Both E_{WV} and E_{C} are positive, implying that the changes in the water vapour amount and cloud amount reduce the amount of the SW decrease by SRM. Temperature reduction decreases the amount of evaporation compared with the RCP4.5 scenario and results in less water vapour in the atmosphere (Kravitz et al., 2013c). Less water vapour may cause reduced cloud amounts; less water vapour and reduced cloud amounts increase the atmospheric SW transmissivity and reduce the SRM's cooling effect. The strengths of E_{WV} and E_{C} are comparable in each model except MIROC-ESM-CHEM-AMP (a reason for this exception is discussed in the next subsection). After SRM termination, E_{WV} remains positive for one or two decades. This is consistent with changes in ΔT shown by the dashed curves; i.e., the water vapour amount in G4 remains less than that in RCP4.5 for a while after the termination. The inter-annual variability of E_{C} is much larger than that of E_{WV}, and the gradual transition to the state of RCP4.5 after the termination (like E_{WV}) is not apparent. Through the whole simulation period, the inter-annual variability of E_{C} dominates that of $\Delta F_{\mathrm{SURF}}^{\mathrm{net}}$. It should be noted that the phases in wave-like, year-to-year variability of $\Delta F_{\mathrm{SURF}}^{\mathrm{net}}$ and ΔT (shown by black solid line and dashed line in Fig. 4) do not agree, although time-averaged $\Delta F_{\mathrm{SURF}}^{\mathrm{net}}$ is well correlated with ΔT as shown in Fig. 3. This is because of thermal inertia and nonlinearities in the Earth system.

3.3 Inter-model dispersion of global mean forcing and SW total reactions

For the inter-model comparison of the results, the global means of F_{SRM}, E_{WV}, E_{C}, and E_{SA} are averaged over the period 2040–2069. Figure 5 shows the relationship between these values (y-axis) and ΔT (x-axis) in the same manner as Fig. 3; $\Delta F_{\mathrm{SURF}}^{\mathrm{net}}$ is shown again. The mean values of F_{SRM} (shown by red symbols) vary widely from approximately -3.6 to -1.6 W m^{-2}, depending on the model. The cooling effect of F_{SRM} in each member or the ensemble mean is reduced by E_{WV} (orange) and E_{C} (blue) and is slightly increased by E_{SA} (green). The net effect is approximately equal to $\Delta F_{\mathrm{SURF}}^{\mathrm{net}}$ (black), which is strongly correlated with ΔT; the residual is less than 0.06 W m^{-2}. This supports the validity of the decomposition of $\Delta F_{\mathrm{SURF}}^{\mathrm{net}}$ into SRM forcing and the total reactions due to changes in the water vapour amount, cloud amount, and surface albedo.

The two models with sulphate aerosol calculation (HadGEM2-ES and MIROC-ESM-CHEM-AMP) show stronger F_{SRM} than the others. This outcome indicates that the prescribed AOD, which is based on one-fourth of the Mount Pinatubo eruption, likely underestimates the AOD that results from actual SO$_2$ injection at a rate of 5 Tg yr^{-1}. It is the difference in the mean AOD rather than its meridional distribution as shown in Fig. S1 that leads to the underestimation of the AOD in G4. The globally and temporally averaged stratospheric sulphate AOD in MIROC-ESM-CHEM-AMP is 0.083 and that in HadGEM2-ES is approximately 0.054, though that of the prescribed AOD is 0.037. Note that the above value for HadGEM2-ES is the difference (G4 $-$ RCP4.5) in the sulphate AOD for both troposphere and stratosphere because HadGEM2-ES does not calculate the sulphate aerosols in the tropospheric and stratosphere separately.

In CanESM2 and MIROC-ESM-CHEM, the F_{SRM} values are very similar among the ensemble members shown by unfilled red symbols. This is consistent with the fact that the given AOD fields for mimicking the SO$_2$ injection effects in G4 are identical among ensemble members of each model. On the other hand, the values of F_{SRM} in the ensemble members of HadGEM2-ES have considerable differences, because the distribution of the sulphate AOD is affected by the chaotic nature of transport and various other processes in the ESM. Even after averaging over 30 years, the mean seasonal cycles of the sulphate AOD can differ among the ensemble members as shown in Fig. S1.

Pitari et al. (2014) have shown that SW radiative forcing at the tropopause calculated off-line by a radiative transfer code (Chou and Suarez, 1999; Chou et al., 2001) varies from around -2.1 to -1.0 W m^{-2} between the models. Since both the analysis methods and the participating models presented here differ from those of Pitari et al., it is difficult to compare the two results. However, the results ($F_{\mathrm{SRM}} \sim -3.6$ to -1.6 W m^{-2}) show that model dependence of the SRM forcing might be larger than that shown by Pitari et al.

Figure 5 shows that E_{WV} is strongly anti-correlated with ΔT; the correlation coefficient for the filled symbols is -0.94. In contrast, E_{C} seems to have no correlation with ΔT, with a correlation coefficient of 0.01. This result shows that the SW total reaction from the change in water vapour amount is much simpler (i.e., almost linear with ΔT across all models) than that from changing the cloud amount, which depends strongly on the cloud parameterization scheme. Furthermore, the results of the ensemble members of CanESM2 and MIROC-ESM-CHEM show that the variation in E_{C} mainly causes the variation in $\Delta F_{\mathrm{SURF}}^{\mathrm{net}}$, which is well correlated with ΔT, though F_{SRM} is same among the members. Thus, among the ensemble members, higher E_{C} seems to bring less cooling. MIROC-ESM-CHEM-AMP marks the strongest forcing of the SRM among the models

but also marks the largest increase of SW from changing the cloud amount. Accordingly, this model shows the moderate values in $\Delta F_{\mathrm{SURF}}^{\mathrm{net}}$ and ΔT; a possible explanation is given in the following analysis.

To compare ratios of the total reaction and the surface cooling to the magnitude of the SRM forcing, E_{WV}, E_{C}, E_{SA}, and ΔT by $|F_{\mathrm{SRM}}|$ are normalized, as shown in Fig. 6. This figure shows the approximate sensitivity of each total reaction per unit forcing of SRM (y-axis) and the normalized surface cooling (x-axis). The value range of $E_{\mathrm{C}}/|F_{\mathrm{SRM}}|$ (0.19–0.55, blue) is significantly wider than that of $E_{\mathrm{WV}}/|F_{\mathrm{SRM}}|$ (0.27–0.42, orange) and that of $E_{\mathrm{SA}}/|F_{\mathrm{SRM}}|$ (−0.12 to −0.06, green). In addition, the three MIROC-based models show higher $E_{\mathrm{C}}/|F_{\mathrm{SRM}}|$ (0.34–0.55) than other three models (0.19–0.34). This means that the sensitivity of the total reaction due to change in cloud amount in the MIROC-based models is higher than other models. This may be why MIROC-ESM-CHEM-AMP, whose $E_{\mathrm{C}}/|F_{\mathrm{SRM}}|$ is as high as those of MIROC-ESM and MIROC-ESM-CHEM, exhibits high E_{C} and yields moderate cooling, although F_{SRM} is very strong, as shown by the cross sign in Fig. 5. That is, high sensitivity of E_{C} to the SRM forcing will weaken the cooling of surface air temperature as well as $\Delta F_{\mathrm{SURF}}^{\mathrm{net}}$.

The wide variability of $E_{\mathrm{C}}/|F_{\mathrm{SRM}}|$ among the models implies a large uncertainty in the models' cloud processes. Moreover, the spread of $E_{\mathrm{C}}/|F_{\mathrm{SRM}}|$ among nine ensemble members of MIROC-ESM-CHEM is also large. The variability among the ensemble members implies that the cloud amount is considerably affected by the chaotic properties and high sensitivity to the initial state of the Earth system or ESM. This result therefore suggests that the cooling of the surface air temperature by the SRM depends significantly on the initial state through total reaction due to changes in the cloud amount.

3.4 Decomposition of total reaction into rapid adjustment and feedback

The total reactions due to changes in water vapour amounts, cloud amounts, and surface albedo discussed in the previous two subsections are the sums of the rapid adjustment, which are independent of ΔT, and the feedback, which depends linearly on ΔT. In this subsection, we attempt to decompose the rapid adjustment and the feedback using a so-called Gregory plot (Gregory et al., 2004). Figure 7 shows globally and annually averaged E_{WV}, E_{C}, and E_{SA} as a function of averaged ΔT for each model. Now, we consider that a slope and a y-intercept show a feedback parameter and an amount of rapid adjustment, respectively, as shown by Eqs. (15)–(17); these values and correlation coefficients are shown in Table 2. The multi-model mean values are also shown.

There are no qualitative inter-model differences and each model has the following properties. E_{WV} (orange $\diamond$) shows high negative correlation with ΔT, and the rapid adjustment and the feedback are clearly separated. In the multi-model mean, the rapid adjustment is -0.30 Wm^{-2} and the feedback parameter is -0.91 $\mathrm{Wm}^{-2}\mathrm{K}^{-1}$.

Unlike E_{WV}, E_{C} (blue $+$) is not well-correlated with ΔT. In addition, the spread of the blue plots is large. This means that the rapid adjustment due to cloud changes varies largely, depending on the simulated state of ESM. The feedback of SW cloud radiative effect is not dominant in G4 experiment. Such positive and large rapid adjustment due to the cloud changes and the small cloud feedback are consistent with Kravitz et al. (2013c), who analysed the GeoMIP-G1 experiment.

The y-intercept of E_{SA} (green $\times$) is almost zero, so that the rapid adjustment from the surface albedo change is negligible. The feedback parameter is 0.38 $\mathrm{Wm}^{-2}\mathrm{K}^{-1}$ in the multi-model mean, and the strength (absolute value) of the feedback is less than a half of that of E_{WV}.

3.5 Robust features in geographical distribution

To explore robust features in the effects of the SRM in G4, the multi-model mean of the surface air temperature and net SW at the surface is calculated. Figures 8a and 8b show ΔT and $\Delta F_{\mathrm{SURF}}^{\mathrm{net}}$ averaged over the period 2040–2069; hatching indicates regions where 2 or more (out of 6) models disagreed on the sign of the difference. The zonal means are shown in the right-hand side panel for each variable (black indicates the multi-model mean, and coloured lines indicate the ensemble mean of each model). Here, model grid intervals are equal to or narrower than 2.8125 deg, so that the geographical regions mentioned below are represented by enough grid points. However, properties of the Sea of Okhotsk and Hudson Bay may depend on related channels, which may be not well resolved. The geographical distribution of the multi-model mean shows that cooling of the surface air temperature is very strong in and around the Arctic Region, except for Greenland and Europe, and stronger on land than over the ocean in other regions. Such features agree with previous studies such as Robock et al. (2008). Reduction of $F_{\mathrm{SURF}}^{\mathrm{net}}$ is strong in the eastern part of Southern Africa, Tibet, East Asia, Sea of Okhotsk, Hudson Bay, and South America. In contrast, $F_{\mathrm{SURF}}^{\mathrm{net}}$ increased compared with RCP4.5 in the equatorial region of the Western Pacific, Southern Ocean, except near the Antarctic coast and northern part of the Atlantic. The above reduction and increase are mainly due to E_{C} and E_{SA}; details will be discussed later in this section. The spatial distribution of the sign of $\Delta F_{\mathrm{SURF}}^{\mathrm{net}}$ varies, whereas ΔT is negative over the whole globe. Although ΔT and $\Delta F_{\mathrm{SURF}}^{\mathrm{net}}$ are correlated in the global mean (Fig. 3), the spatial distribution of ΔT does not necessarily need to agree with that of $\Delta F_{\mathrm{SURF}}^{\mathrm{net}}$ because circulation and hydrological processes transport and redistribute energy.

Qualitatively opposite geographical features in ΔT and $\Delta F_{\mathrm{SURF}}^{\mathrm{net}}$ appear in the simulated climate change in RCP4.5 shown in Figs. 8c and 8d, calculated as the difference between the 2010–2039 average and the 2040–2069 average of the RCP4.5 data. Note that the very high positive value in East Asia in Fig. 8d is due to a large reduction of anthropogenic aerosol emission assumed in the late 21st century in the RCP4.5 scenario (Thomson et al., 2011; Westervelt et al., 2015). With the exception of the effects of such assumed emission reduction, sulphate geoengineering can delay global warming almost without regional biases; that is, regions where surface air temperature increases are relatively high in RCP4.5 undergo a large amount of cooling by the sulphate geoengineering and regions with a relatively low increases in temperature receive a small amount of cooling. Model dependence in ΔT shown by coloured lines in Fig. 8a is relatively large in high latitudes in the Northern Hemisphere but small (i.e., comparable with the spread of the global mean ΔT) in other regions. For $\Delta F_{\mathrm{SURF}}^{\mathrm{net}}$ shown in Fig. 8b, all models show qualitatively similar average features at least in the zonal mean, and the range is about $\pm 0.75\ \mathrm{W\,m^{-2}}$.

Next, the multi-model mean of global distributions (averaged over 2040–2069) of (a) F_{SRM}, (b) E_{WV}, (c) E_{C}, and (d) E_{SA} are calculated, as shown in Fig. 9. The SRM forcing is relatively weak in the regions where the annual mean surface albedo is high, such as Greenland, the Sahara, the Middle East, Australia, and Antarctica. This is mainly because the net SW at the surface is low due to the high surface albedo, and accordingly the absolute value of the SRM forcing becomes low. This can be shown via low order approximation: the net SW at the surface can be written as $F_{\mathrm{SURF}}^{\mathrm{net}} \approx (1-\alpha)S(1-R-A)$, and the SRM forcing can be approximated as $F_{\mathrm{SRM}} \approx -(1-\alpha_{\mathrm{RCP}})S(R_{\mathrm{G4}}^{\mathrm{cs}} - R_{\mathrm{RCP}}^{\mathrm{cs}})$, whose absolute value becomes small when α_{RCP} is high. Except for these high surface-albedo regions, the spatial variation in SRM forcing is not very large, even though the incoming

solar radiation is strong at low latitudes and weak at high latitudes. This is because the atmospheric reflection rate depends on the solar zenith angle, and the reflection rate becomes higher as the zenith angle increases (e.g., Joseph et al., 1976). That is, strong solar radiation at low latitudes is reflected with low efficiency and weak solar radiation at the high latitudes is reflected with high efficiency. Accordingly, the latitudinal distribution of the SRM forcing is close to uniform in many models. The above feature is a notable aspect in sulphate geoengineering compared with idealized SRM experiments such as G1 and G2, in which the solar constant is simply reduced (Kravitz et al., 2013a) and the forcing is proportional to the cosine of latitude. Latitudinal distribution of F_{SRM} in HadGEM2-ES (purple line in Fig. 9a) and MIROC-ESM-CHEM-AMP (red line in Fig. 9a) shows a stronger latitudinal dependence. These results are consistent with the (approximate) distribution of the stratospheric sulphate AOD as shown in Fig. S1.

The SW total reaction due to the change in the water vapour amount (Fig. 9b) is close to uniform compared with that of the cloud amount (Fig. 9c). The slight increase of E_{WV}, which implies less water vapour, in the equatorial region is consistent of decrease of precipitation reported by Rasch et al. (2008a) and Robock et al. (2008) under SRM. E_{C} has a large spatial variability, which yields many of the spatial variation of $\Delta F_{\text{SURF}}^{\text{net}}$, such as positive values in the equatorial region of the Western Pacific, the Southern Ocean, and the northern part of the Atlantic, and negative values in the eastern part of the Southern Africa, East Asia, and South America. Because $\Delta F_{\text{SURF}}^{\text{net}}$ (Fig. 8b) and the simulated climate change of $F_{\text{SURF}}^{\text{net}}$ in RCP4.5 (Fig. 8d) are opposite in sign, the above result suggests that the SRM offsets increases in the cloud amount simulated in the RCP4.5 scenario, in the positive regions in Fig. 9c and vice versa in the negative regions. The remaining features in $\Delta F_{\text{SURF}}^{\text{net}}$ are caused by the effect of surface albedo change (Fig. 9d), which has large negative values in Tibet, the Sea of Okhotsk, Hudson Bay, and the Southern Ocean near the Antarctic coast. That is, snow and sea ice remain in these regions in the G4 experiment because of the SRM. At high latitudes, the decrease of the net SW at the surface by the change in surface albedo is as large as the SW increase by the change in cloud amount (see the line graph in panels c and d), although E_{SA} is minor in the global mean.

4 Discussion

4.1 Difference between the surface and TOA

This study has focused on the surface net SW because of its importance to human activities. However, the situation at TOA is also of interest. Now, we discuss how the measures used in this study differ when TOA is used for the analysis. The net SW at TOA can be written as

$$F_{\text{TOA}}^{\text{net}} \equiv S - F_{\text{TOA}}^{\uparrow \text{as}} = S \left\{ 1 - (R^{\text{cs}} + R^{\text{cl}}) - \alpha \frac{\left[1 - (R^{\text{cs}} + R^{\text{cl}}) - (A^{\text{cs}} + A^{\text{cl}}) \right]^2}{1 - \alpha (R^{\text{cs}} + R^{\text{cl}})} \right\}, \tag{18}$$

so that the direct forcing of SRM and the total reactions measured at TOA ($F_{\text{SRM}}^{\text{TOA}}$, $E_{\text{WV}}^{\text{TOA}}$, $E_{\text{C}}^{\text{TOA}}$, and $E_{\text{SA}}^{\text{TOA}}$) can be calculated in the same manner described in Section 2. Figure 10 shows their globally and temporally averaged values' dependencies on ΔT. The difference of $F_{\text{TOA}}^{\text{net}}$ is also plotted.

The qualitative features of the measures other than $E_{\mathrm{WV}}^{\mathrm{TOA}}$ are same as the analysis at the surface shown in Fig. 6. The quantitative difference in the SRM forcing ($F_{\mathrm{SRM}}^{\mathrm{TOA}} - F_{\mathrm{SRM}}$) is as small as $-0.047\,\mathrm{Wm}^{-2}$ (1.8 %) for the multi-model mean. In contrast, $|E_{\mathrm{SA}}^{\mathrm{TOA}}|$ is less than that of $|E_{\mathrm{SA}}|$ by about 35 %. This is because the upward shortwave radiation that was reflected at the surface must pass the atmosphere being decreased by absorption and reflection before reaching the TOA. The difference of $E_{\mathrm{C}}^{\mathrm{TOA}} - E_{\mathrm{C}}$ is $0.12\,\mathrm{Wm}^{-2}$ (16.5 %) for the multi-model mean. Remember that the effect of the cloud amount change includes both changes in reflection rate (R^{cl}) and absorption rate (A^{cl}). The effect of a change in R^{cl} should appear almost equally at the surface and TOA, as the case for the SRM forcing, because both R^{cl} and R^{cs} appear in the Eqs. (7) and (18) in the same way. Therefore, most of $E_{\mathrm{C}}^{\mathrm{TOA}} - E_{\mathrm{C}}$ should be caused by the difference in how the change of the absorption rate affects the net SW at the surface and that at TOA. This is discussed below.

The total reaction at TOA due to the change in water vapour amount shows a negative sign, which is opposite to that at the surface. This disagreement is attributed as follows: Surface cooling reduces the amount of water vapour in the atmosphere and the SW absorption rate decreases. Then, more incoming solar radiation reaches the surface, so that the decrease in water vapour amount increases SW flux at the surface. On the other hand, when the SW absorption rate decreases, the more upwelling SW that was reflected at the surface pass through the atmosphere and reaches TOA. This leads to a cooling effect. Because the effect of decrease in the SW absorption rate is carried to TOA by the upwelling SW that was reflected at the surface by the rate of α, $|E_{\mathrm{SA}}^{\mathrm{TOA}}|$ it is much less than $|E_{\mathrm{SA}}|$. This does not mean that the change in water vapour is negligible for the energy budget at TOA, because we have not explored LW in this study. An analysis on LW rapid adjustment of clear-sky is discussed in the next subsection, but that of clouds and LW feedback is left as our future work.

From the above discussion, we have found that the effect of changes in atmospheric SW absorption rate appears differently between at the surface and at TOA (in its sign and amount), but that in reflection rate appears almost equally. The effect of change in the surface albedo is weaker at TOA than at the surface. We will bear these properties in our mind, when we discuss the influence of SRM on the energy budget of the climate system, which is usually considered at TOA, and human activities, which are mainly performed at the surface.

4.2 Rapid adjustment of longwave radiation

This study has concentrated on SW for the reasons described in Section 1; however, it may be valuable for some readers to mention the role of LW. A well-known effect of LW in sulphate aerosol geoengineering is heating of the stratosphere. The sulphate aerosols induced by the SO_2 injection absorb LW and heat air in the lower the stratosphere (e.g., Heckendorn et al., 2009; Pitari et al., 2014). For the energy budget at TOA, increase of the LW absorption results in decrease of the outgoing LW, which manifests as a heating of the climate system. Needless to say, there are many interactions among LW, temperature, and various other components of the climate system through the emission and absorption of LW. Because of such complexity, unlike the SW changes that we have explored in this study, it is difficult to distinguish and estimate the effect of each factor on LW changes.

One possible and useful analysis for LW is to estimate the rapid adjustment (or response), which is independent of ΔT, by the same method used in Section 3.4. Gregory-like plots are made for the difference of net LW for clear-sky at the surface

(ΔLW^{cs}_{SURF}) and at TOA (ΔLW^{cs}_{TOA}) as shown by black "+" signs and red "×" signs, respectively, in Fig. 11. The rapid adjustment in the clear-sky at the TOA shown by the y-intercept of the ΔLW^{cs}_{TOA} regression line shows a heating effect of about 0.57 Wm^{-2} in the multi-model mean. This rapid adjustment should mainly consist of the effect of LW absorption due to stratospheric sulphate aerosols, since the decrease of the water vapour suggested by the rapid adjustment of E_{WV} yields less

5   LW absorption and an increase in outgoing LW at TOA (i.e., sense of cooling). It is important to take this heating effect in mind when we consider the energy budget at TOA for sulphate geoengineering. Though the sulphate aerosols' LW effect is significant at TOA, such effect may be less significant at the surface, because the rapid adjustment estimated from ΔLW^{cs}_{SURF} is small compared to the SRM forcing and total reactions at the surface.

4.3   Inequality in the number of ensemble and participating models

10   One concern in this study is that half of the models used have only one ensemble member, and half are MIROC-based models. Because the numbers of ensemble members differ among models as listed in Table 1, each member in each model is not equally weighted in calculation of the multi-model means described in Section 3.5. Responses to the SRM forcing in the three MIROC-based models should be similar to each other as shown in Fig. 6, so that the results of multi-model mean can be biased to that of the MIROC-based models. Therefore, we re-calculated multi-model means by using only one run for each model (Fig. S2); and

15   also tested multi-model means with a weight of 1/3 for the MIROC-based models (Fig. S3). There are no significant difference among Figs. 9, S2, and S3. Therefore, inequality in the number of ensemble and participating models has no significant effects on our results.

5   Summary and concluding remarks

The results from six models (listed in Table 1) that simulated GeoMIP experiment G4, which is designed to simulate sulphate

20   geoengineering by injecting 5 Tg of SO_2 into the stratosphere every year from 2020 to 2070 in the RCP4.5 scenario as the baseline, have been analysed. A single-layer model proposed by Donohoe and Battisti (2011) has been applied to estimate the strength and its inter-model variability of the SRM forcing (F_{SRM}) to the surface net shortwave radiation, whose difference between G4 and RCP4.5 (ΔF^{net}_{SURF}) has a strong correlation with the cooling of the surface air temperature (ΔT), as shown in Fig. 3. The SW total reactions due to changes in the water vapour amount (E_{WV}), cloud amount (E_C), and surface albedo

25   (E_{SA}) have been also estimated. Here, a total reaction is defined as a sum of a rapid adjustment, which does not depend on ΔT, and a feedback, which is proportional to ΔT. Decomposition of the estimated total reactions into the rapid adjustment and the feedback is also done by using a method based on the Gregory plot (Gregory et al., 2004). Note that, unlike the usual Gregory plot, ΔT is defined by the difference between T_{G4} and T_{RCP}, and both experiments are not approaching a statistically equilibrium state, so that the rapid response could vary depending on the state of the modelled climate system.

30   It has been shown that the globally and temporally averaged F_{SRM} of each model varies widely from about -3.6 to -1.6 $W\,m^{-2}$ (red symbols in Fig. 5). Inter-model variations comprise a substantial range, and narrowing this uncertainty is essential for understanding the effects of sulphate geoengineering and its interactions with chemical, micro-physical, dynamical, and

radiative processes related to the formation, distribution, and shortwave-reflectance of the sulphate aerosols introduced from the SO_2 injection (Rasch et al., 2008b; Kremser et al., 2016).

Our analysis has also shown that, in the global average, changes in the water vapour and cloud amounts (from RCP4.5) increase the SW at the surface and reduce the effect of F_{SRM} by approximately 0.4–$1.2\,\mathrm{W\,m^{-2}}$ and 0.5–$1.5\,\mathrm{W\,m^{-2}}$, respec-
tively. This is due to the smaller amounts of water vapour and clouds, which mainly block the downwelling solar radiation from reaching the surface by absorption and reflection, respectively. E_{WV} is well correlated with ΔT in multi-model comparison, whereas E_C is not. The reduction rate of E_C varies from 19 % to 55 % as compared to F_{SRM} depending on both models and ensemble runs (i.e., initial states), whereas that of E_{WV} is 27–42 %. The effect of surface albedo changes is small in the global average, but is significant in the regions where snow or ice melts in the RCP4.5 scenario.

The decomposition analysis has revealed that about 37 % (multi-model mean) of E_{WV} is explained by the rapid adjustment and the rest is the feedback. On the other hand, almost all of E_C consists of the rapid adjustment, and a linear relationship between E_C and ΔT for the global and annual mean was not obtained for any models. The cloud rapid adjustment in G4 deduced in this study is similar as found for G1 by Kravitz et al. (2013c) but disagree with that in the 4xCO2 experiment shown by Andrews et al. (2012). Because the rapid adjustment due to changes in clouds can be caused by various processes
(e.g., changes in atmospheric stability), it is possible that the cloud rapid adjustment differs between SRM and global warming. More detailed studies on cloud processes in SRM are required for the reduction of the uncertainty and for a better assessment of impact of the sulphate geoengineering on climate and human activities.

The multi-model mean horizontal distribution of ΔT suggests that stratospheric sulphate aerosol geoengineering can delay global warming without significant regional biases, unlike the results of the GeoMIP-G1 experiment (Kravitz et al., 2013a). In
G1, the incoming solar radiation was just reduced by a constant fraction, so that the SRM forcing has large latitudinal variation (strong in low-latitudes and weak in high-latitudes). Conversely, in G4, the distribution of sulphate aerosol optical depth (AOD) is internally calculated or externally given, and the reflection of the solar radiation is locally calculated. Here, at least for the prescribed AOD calculated from observed AOD after the 1991 Mount Pinatubo eruption, sulphate aerosols are assumed to spread out globally and form a somewhat uniform distribution as shown in Fig. 1. Because the reflection rate, as well as the
incoming solar radiation, depends on the solar zenith angle, as described previously, the resultant SRM forcing does not have large latitudinal variation, as shown in Fig. 9a.

This study has the following three limitations. First, the single-layer model used treats the reflection of downward radiation and that of upward radiation by the same rate. As noted above, however, the reflection rate depends on the incident angle, so errors could be significant in regions that have high solar zenith angle and high surface albedo, such as Greenland and
Antarctica.

Second, the SW absorption by the sulphate aerosols has been ignored, because its amount is considered minor compared to the SW reflection. If the absorption by the sulphate aerosols is non-negligible, E_{WV} should be regarded as the sum of a part of SRM forcing by absorption and total reaction due to the change in the water vapour amount, and the forcing and total reaction are not well separated from each other. At least for MIROC-ESM-CHEM, this study confirms that the influence
of SW absorption by the sulphate aerosols on E_{WV} is less than 4.5 % by performing the G4 experiment with vanishing SW

absorption coefficients of the sulphate aerosols. In other words, the SRM forcing due to SW absorption by the sulphate aerosols is less than 1.5 % of that due to reflection (F_{SRM}). The magnitude of errors in the other models should be similar to that in MIROC-ESM-CHEM.

Finally, SW at the surface has been the focus of this analysis and the energy balance has not been considered. ΔT can be affected by other types of rapid adjustment and feedback. For example, the reduced water vapour in G4 causes less SW absorption by the atmosphere and cooling of the troposphere. The greenhouse effect due to the water vapour would be also decreased. Then, in total, the effect of change in water vapour amount may be a cooling effect (i.e., a positive feedback). However, further analysis is required to separate the effect of water vapour from the LW flux. Analyses of the full energy balance and other types of feedback will form part of future work.

6   Data availability

All data used in this study, except for the data of MIROC-ESM-CHEM-AMP, are available through the Earth System Grid Federation (ESGF) Network (http://esgf.llnl.gov). The data of MIROC-ESM-CHEM-AMP are available by contacting the corresponding author.

Author contributions.   HK, MA, SW, and TS analysed the data. SW, TS, DJ, JM, and JC developed the models and performed the experiment. BK designed and organized the experiment. All authors contributed to the discussion.

The authors declare that they have no conflict of interest.

Acknowledgements.   We thank Dr. Aaron Donohoe and an anonymous reviewer for useful comments, which greatly help us to improve the manuscript. We thank all participants of the Geoengineering Model Intercomparison Project and their model development teams, CLI-VAR/WCRP Working Group on Coupled Modelling for endorsing GeoMIP, and the scientists managing the Earth System Grid data nodes who have assisted with making GeoMIP output available. We thank Drs. Charles Curry, James M. Haywood, and Andy Jones for model development and comments on the manuscript. We also thank Drs. Masahiro Sugiyama, Hideo Shiogama, and Seita Emori for useful comments. HK, MA, and SW were supported by the SOUSEI Program, MEXT, Japan. Simulations of MIROC-based models were conducted using the Earth Simulator. The Pacific Northwest National Laboratory is operated for the U.S. Department of Energy by Battelle Memorial Institute under contract DE-AC05-76RL01830.

References

Andrews, T., Gregory, J. M., Webb, M. J., and Taylor, K. E.: Forcing, feedbacks and climate sensitivity in CMIP5 coupled atmosphere-ocean climate models, Geophys. Res. Lett., 39, L09 712, 2012.

Arora, V. K. and Boer, G. J.: Uncertainties in the 20th century carbon budget associated with land use change, Glob. Change Biol., 16, 3327–3348, 2010.

Arora, V. K., Scinocca, J. F., Boer, G. J., Christian, J. R., Denman, K. L., Flato, G. M., Kharin, V. V., Lee, W. G., and Merryfield, W. J.: Carbon emission limits required to satisfy future representative concentration pathways of greenhouse gases, Geophys. Res. Lett., 38, L05805, 2011.

Bala, G., Duffy, P. B., and Taylor, K. E.: Impact of geoengineering schemes on the global hydrological cycle., P. Natl. Acad. Sci. USA, 105, 7664–7669, 2008.

Bellouin, N., Rae, J., Jones, A., Johnson, C., Haywood, J., and Boucher, O.: Aerosol forcing in the Climate Model Intercomparison Project (CMIP5) simulations by HadGEM2-ES and the role of ammonium nitrate, J. Geophys. Res., 116, D20 206, 2011.

Budyko, M. I.: Climate and life, Academic Press, New York, 1974.

Chou, M. D. and Suarez, M. J.: A solar radiation parameterization for atmospheric studies, Tech. Rep. TM-1999-104606, NASA Goddard Space Flight Center, Greenbelt, MD, 1999.

Chou, M.-D., Suarez, M. J., Liang, X.-Z., Yan, M. M. H., and Cote, C.: A thermal infrared radiation parameterization for atmospheric studies, Tech. Rep. TM-2001-104606, NASA Goddard Space Flight Center, Greenbelt, MD, 2001.

Collins, W. J., Bellouin, N., Doutriaux-Boucher, M., Gedney, N., Halloran, P., Hinton, T., Hughes, J., Jones, C. D., Joshi, M., Liddicoat, S., Martin, G., O'Connor, F., Rae, J., Senior, C., Sitch, S., Totterdell, I., Wiltshire, A., and Woodward, S.: Development and evaluation of an Earth-System model – HadGEM2, Geosci. Model Dev., 4, 1051–1075, 2011.

Colman, R.: A comparison of climate feedbacks in general circulation models, Clim. Dynam., 20, 865–873, 2003.

Crutzen, P. J.: Albedo enhancement by stratospheric sulfur injections: A contribution to resolve a policy dilemma?, Climatic Change, 77, 211–220, 2006.

Donohoe, A. and Battisti, D. S.: Atmospheric and surface contributions to planetary albedo, J. Climate, 24, 4402–4418, 2011.

Govindasamy, B. and Caldeira, K.: Geoengineering Earth's radiation balance to mitigate CO_2-induced climate change, Geophys. Res. Lett., 27, 2141–2144, 2000.

Govindasamy, B., Thompson, S., Duffy, P. B., Caldeira, K., and Delire, C.: Impact of geoengineering schemes on the terrestrial biosphere, Geophys. Res. Lett., 29, 2002.

Govindasamy, B., Caldeira, K., and Duffy, P. B.: Geoengineering Earth's radiation balance to mitigate climate change from a quadrupling of CO_2, Global Planet. Change, 37, 157–168, 2003.

Gregory, J. M., Ingram, W. J., Palmer, M. A., Jones, G. S., Stott, P. A., Thorpe, R. B., Lowe, J. A., Johns, T. C., and Williams, K. D.: A new method for diagnosing radiative forcing and climate sensitivity, Geophys. Res. Lett., 31, L03 205, 2004.

Haywood, J. M. and Ramaswamy, V.: Global sensitivity studies of the direct radiative forcing due to anthropogenic sulfate and black carbon aerosols, J. Geophys. Res., 103, 6043–6058, 1998.

Heckendorn, P., Weisenstein, D., Fueglistaler, S., Luo, B. P., Rozanov, E., Schraner, M., Thomason, L. W., and Peter, T.: The impact of geoengineering aerosols on stratospheric temperature and ozone, Environ. Res. Lett., 4, 045 108, 2009.

IPCC: Climate Change 2007: Synthesis Report, Contribution of working groups I, II and III to the Fourth Assessment Report of the Inter-governmental Panel on Climate Change, IPCC, Geneva, 2007.

Ji, D., Wang, L., Feng, J., Wu, Q., Cheng, H., Zhang, Q., Yang, J., Dong, W., Dai, Y., Gong, D., Zhang, R. H., Wang, X., Liu, J., Moore, J. C., Chen, D., and Zhou, M.: Description and basic evaluation of Beijing Normal University Earth System Model (BNU-ESM) version 1, Geosci. Model Dev., 7, 2039–2064, 2014.

Jones, A., Haywood, J., Boucher, O., Kravitz, B., and Robock, A.: Geoengineering by stratospheric SO_2 injection: results from the Met Office HadGEM2 climate model and comparison with the Goddard Institute for Space Studies ModelE, Atmos. Chem. Phys., 10, 5999–6006, 2010.

Jones, A., Haywood, J. M., Alterskjær, K., Boucher, O., Cole, J. N. S., Curry, C. L., Irvine, P. J., Ji, D., Kravitz, B., Egill Kristjánsson, J., Moore, J. C., Niemeier, U., Robock, A., Schmidt, H., Singh, B., Tilmes, S., Watanabe, S., and Yoon, J. H.: The impact of abrupt suspension of solar radiation management (termination effect) in experiment G2 of the Geoengineering Model Intercomparison Project (GeoMIP), J. Geophys. Res.-Atmos., 118, 9743–9752, 2013.

Jones, A. C., Haywood, J. M., and Jones, A.: Climatic impacts of stratospheric geoengineering with sulfate, black carbon and titania injection, Atmos. Chem. Phys., 16, 2843–2862, 2016a.

Jones, A. C., Haywood, J. M., Jones, A., and Aquila, V.: Sensitivity of volcanic aerosol dispersion to meteorological conditions: A Pinatubo case study, J. Geophys. Res.-Atmos., 121, 6892–6908, 2016b.

Joseph, J. H., Wiscombe, W. J., and Weinman, J. A.: The delta-Eddington approximation for radiative flux transfer, J. Atmos. Sci., 33, 2452–2459, 1976.

Kleidon, A., Kravitz, B., and Renner, M.: The hydrological sensitivity to global warming and solar geoengineering derived from thermody-namic constraints, Geophys. Res. Lett., 42, 138–144, 2015.

Kravitz, B., Robock, A., Boucher, O., Schmidt, H., Taylor, K. E., Stenchikov, G., and Schulz, M.: The Geoengineering Model Intercomparison Project (GeoMIP), Atmos. Sci. Lett., 12, 162–167, 2011.

Kravitz, B., Caldeira, K., Boucher, O., Robock, A., Rasch, P. J., Alterskjær, K., Karam, D. B., Cole, J. N. S., Curry, C. L., Haywood, J. M., Irvine, P. J., Ji, D., Jones, A., Kristjánsson, J. E., Lunt, D. J., Moore, J. C., Niemeier, U., Schmidt, H., Schulz, M., Singh, B., Tilmes, S., Watanabe, S., Yang, S., and Yoon, J. H.: Climate model response from the Geoengineering Model Intercomparison Project (GeoMIP), J. Geophys. Res.-Atmos., 118, 8320–8332, 2013a.

Kravitz, B., Forster, P. M., Jones, A., Robock, A., Alterskjær, K., Boucher, O., Jenkins, A. K. L., Korhonen, H., Kristjánsson, J. E., Muri, H., Niemeier, U., Partanen, A.-I., Rasch, P. J., Wang, H., and Watanabe, S.: Sea spray geoengineering experiments in the geoengineering model intercomparison project (GeoMIP): Experimental design and preliminary results, J. Geophys. Res.-Atmos., 118, 11,175–11,186, 2013b.

Kravitz, B., Rasch, P. J., Forster, P. M., Andrews, T., Cole, J. N. S., Irvine, P. J., Ji, D., Kristjánsson, J. E., Moore, J. C., Muri, H., Niemeier, U., Robock, A., Singh, B., Tilmes, S., Watanabe, S., and Yoon, J. H.: An energetic perspective on hydrological cycle changes in the Geoengineering Model Intercomparison Project, J. Geophys. Res.-Atmos., 118, 13,087–13,102, 2013c.

Kravitz, B., Robock, A., Forster, P. M., Haywood, J. M., Lawrence, M. G., and Schmidt, H.: An overview of the Geoengineering Model Intercomparison Project (GeoMIP), J. Geophys. Res.-Atmos., 118, 13,103–13,107, 2013d.

Kremser, S., Thomason, L. W., Hobe, M., Hermann, M., Deshler, T., Timmreck, C., Toohey, M., Stenke, A., Schwarz, J. P., Weigel, R., Fueglistaler, S., Prata, F. J., Vernier, J. P., Schlager, H., Barnes, J. E., Antuña Marrero, J. C., Fairlie, D., Palm, M., Mahieu, E., Notholt, J., Rex, M., Bingen, C., Vanhellemont, F., Bourassa, A., Plane, J. M. C., Klocke, D., Carn, S. A., Clarisse, L., Trickl, T., Neely, R., James,

A. D., Rieger, L., Wilson, J. C., and Meland, B.: Stratospheric aerosol—Observations, processes, and impact on climate, Rev. Geophys., 54, 278–335, 2016.

Lane, L., Caldeira, K., Chatfield, R., and Langhoff, S., eds.: Workshop report on managing solar radiation, 2007.

Matthews, H. D. and Caldeira, K.: Transient climate–carbon simulations of planetary geoengineering, P. Natl. Acad. Sci. USA, 104, 9949–9954, 2007.

Moore, J. C., Rinke, A., Yu, X., Ji, D., Cui, X., Li, Y., Alterskjær, K., Kristjánsson, J. E., Muri, H., Boucher, O., Huneeus, N., Kravitz, B., Robock, A., Niemeier, U., Schulz, M., Tilmes, S., Watanabe, S., and Yang, S.: Arctic sea ice and atmospheric circulation under the GeoMIP G1 scenario, J. Geophys. Res.-Atmos., 119, 567–583, 2014.

Niemeier, U. and Timmreck, C.: What is the limit of climate engineering by stratospheric injection of SO_2?, Atmospheric Chemistry and Physics, 15, 9129–9141, 2015.

Parker, D. E., Wilson, H., Jones, P. D., Christy, J. R., and Folland, C. K.: The impact of mount Pinatubo on world-wide temperatures, Int. J. Climatol., 16, 487–497, 1996.

Phipps, S. J., Rotstayn, L. D., Gordon, H. B., Roberts, J. L., Hirst, A. C., and Budd, W. F.: The CSIRO Mk3L climate system model version 1.0 – Part 1: Description and evaluation, Geosci. Model Dev., 4, 483–509, 2011.

Phipps, S. J., Rotstayn, L. D., Gordon, H. B., Roberts, J. L., Hirst, A. C., and Budd, W. F.: The CSIRO Mk3L climate system model version 1.0 – Part 2: Response to external forcings, Geosci. Model Dev., 5, 649–682, 2012.

Pierce, J. R., Weisenstein, D. K., Heckendorn, P., Peter, T., and Keith, D. W.: Efficient formation of stratospheric aerosol for climate engineering by emission of condensible vapor from aircraft, Geophys. Res. Lett., 37, L18 805, 2010.

Pitari, G., Mancini, E., Rizi, V., and Shindell, D. T.: Impact of future climate and emission changes on stratospheric aerosols and ozone, J. Atmos. Sci., 59, 414–440, 2002.

Pitari, G., Aquila, V., Kravitz, B., Robock, A., Watanabe, S., Cionni, I., Luca, N. D., Genova, G. D., Mancini, E., and Tilmes, S.: Stratospheric ozone response to sulfate geoengineering: Results from the Geoengineering Model Intercomparison Project (GeoMIP), J. Geophys. Res.-Atmos., 119, 2629–2653, 2014.

Rasch, P. J., Crutzen, P. J., and Coleman, D. B.: Exploring the geoengineering of climate using stratospheric sulfate aerosols: The role of particle size, Geophys. Res. Lett., 35, L02809, 2008a.

Rasch, P. J., Tilmes, S., Turco, R. P., Robock, A., Oman, L., Chen, C.-C., Stenchikov, G. L., and Garcia, R. R.: An overview of geoengineering of climate using stratospheric sulphate aerosols, Phil. Trans. R. Soc. A, 366, 4007–4037, 2008b.

Rasool, S. I. and Schneider, S. H.: Atmospheric carbon dioxide and aerosols: Effects of large increases on global climate, Science, 173, 138–141, 1971.

Rienecker, M. M., Suarez, M. J., Todling, R., Bacmeister, J., Takacs, L., Liu, H. C., Gu, W., Sienkiewicz, M., Koster, R. D., Gelaro, R., Stajner, I., and Nielsen, J. E.: The GEOS-5 data assimilation system-documentation of versions 5.0.1, 5.1.0, and 5.2.0, Technical Report Series on Global Modeling and Data Assimilation, 27, 2008.

Robock, A., Oman, L., and Stenchikov, G. L.: Regional climate responses to geoengineering with tropical and Arctic SO_2 injections, J. Geophys. Res., 113, D16101, 2008.

Sato, M., Hansen, J. E., and McCormick, M. P.: Stratospheric aerosol optical depths, 1850–1990, J. Geophys. Res., 98, 22 987–22 994, 1993.

Schmidt, G. A., Ruedy, R., Hansen, J. E., Aleinov, I., Bell, N., Bauer, M., Bauer, S., Cairns, B., Canuto, V., Cheng, Y., Del Genio, A., Faluvegi, G., Friend, A. D., Hall, T. M., Hu, Y., Kelley, M., Kiang, N. Y., Koch, D., Lacis, A. A., Lerner, J., Lo, K. K., Miller, R. L., Nazarenko, L., Oinas, V., Perlwitz, J., Perlwitz, J., Rind, D., Romanou, A., Russell, G. L., Sato, M., Shindell, D. T., Stone, P. H., Sun, S.,

Tausnev, N., Thresher, D., and Yao, M.-S.: Present-day atmospheric simulations using GISS ModelE: Comparison to in situ, satellite, and reanalysis data, J. Climate, 19, 153–192, 2006.

Schmidt, H., Alterskjær, K., Bou Karam, D., Boucher, O., Jones, A., Kristjánsson, J. E., Niemeier, U., Schulz, M., Aaheim, A., Benduhn, F., Lawrence, M., and Timmreck, C.: Solar irradiance reduction to counteract radiative forcing from a quadrupling of CO_2: climate responses simulated by four earth system models, Earth Syst. Dynam., 3, 63–78, 2012.

Sekiya, T., Sudo, K., and Nagai, T.: Evolution of stratospheric sulfate aerosol from the 1991 Pinatubo eruption: Roles of aerosol microphysical processes, J. Geophys. Res.-Atmos., 2016.

Shepherd, J. G.: Geoengineering the climate: science, governance and uncertainty, Royal Society, 2009.

Sherwood, S. C., Bony, S., Boucher, O., Bretherton, C., Forster, P. M., Gregory, J. M., and Stevens, B.: Adjustments in the Forcing-Feedback Framework for Understanding Climate Change, Bull. Amer. Meteorol. Soc., 96, 217–228, 2015.

Soden, B. J., Broccoli, A. J., and Hemler, R. S.: On the use of cloud forcing to estimate cloud feedback, J. Climate, 17, 3661–3665, 2004.

Thomson, A. M., Calvin, K. V., Smith, S. J., Kyle, G. P., Volke, A., Patel, P., Delgado-Arias, S., Bond-Lamberty, B., Wise, M. A., Clarke, L. E., and Edmonds, J. A.: RCP4.5: a pathway for stabilization of radiative forcing by 2100, Climatic Change, 109, 77–94, 2011.

Watanabe, S., Hajima, T., Sudo, K., Nagashima, T., Takemura, T., Okajima, H., Nozawa, T., Kawase, H., Abe, M., Yokohata, T., Ise, T., Sato, H., Kato, E., Takata, K., Emori, S., and Kawamiya, M.: MIROC-ESM 2010: model description and basic results of CMIP5-20c3m experiments, Geosci. Model Dev., 4, 845–872, 2011.

Westervelt, D. M., Horowitz, L. W., Naik, V., Golaz, J. C., and Mauzerall, D. L.: Radiative forcing and climate response to projected 21st century aerosol decreases, Atmos. Chem. Phys., 15, 12 681–12 703, 2015.

Wigley, T. M. L.: A combined mitigation/geoengineering approach to climate stabilization, Science, 314, 452–454, 2006.

Yu, X., Moore, J. C., Cui, X., Rinke, A., Ji, D., Kravitz, B., and Yoon, J. H.: Impacts, effectiveness and regional inequalities of the GeoMIP G1 to G4 solar radiation management scenarios, Global Planet. Change, 129, 10–22, 2015.

Zhang, M. H., Hack, J. J., Kiehl, J. T., and Cess, R. D.: Diagnostic study of climate feedback processes in atmospheric general circulation models, J. Geophys. Res., 99, 5525–5537, 1994.
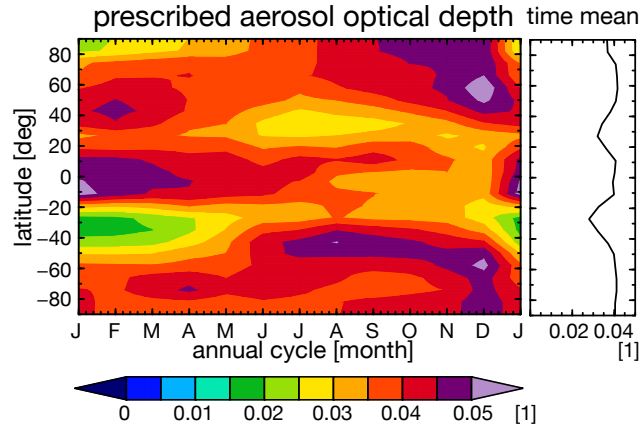
Figure 1. Annual cycle and latitudinal distribution of the prescribed aerosol optical depth provided from the GeoMIP for G4 experiment and used in BNU-ESM, MIROC-ESM, and MIROC-ESM-CHEM. Line graph shows the annual mean.
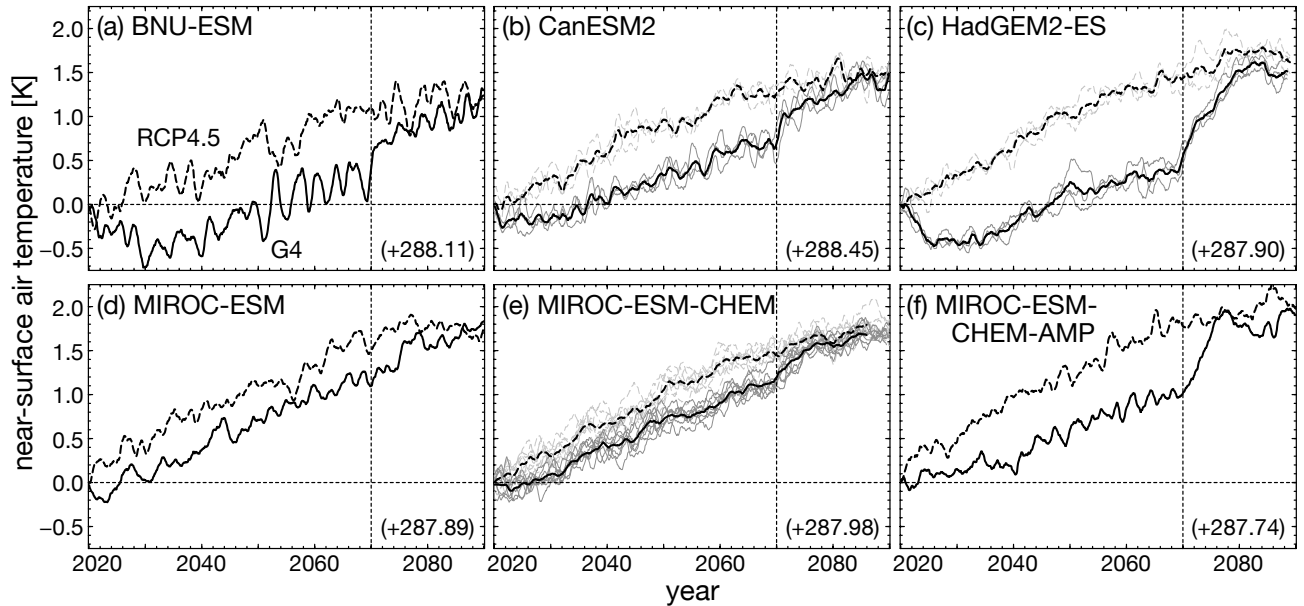
Figure 2. Globally averaged surface air temperature in G4 (solid) and RCP4.5 (dashed) experiments. 12-month running mean is applied. Values are offset by the value at 2020, the beginning of SRM, shown at the right bottom on each panel. In panels (b), (c), and (e), black curves show the ensemble mean and grey curves show ensemble members. The vertical dashed lines indicate the SRM termination (2070).
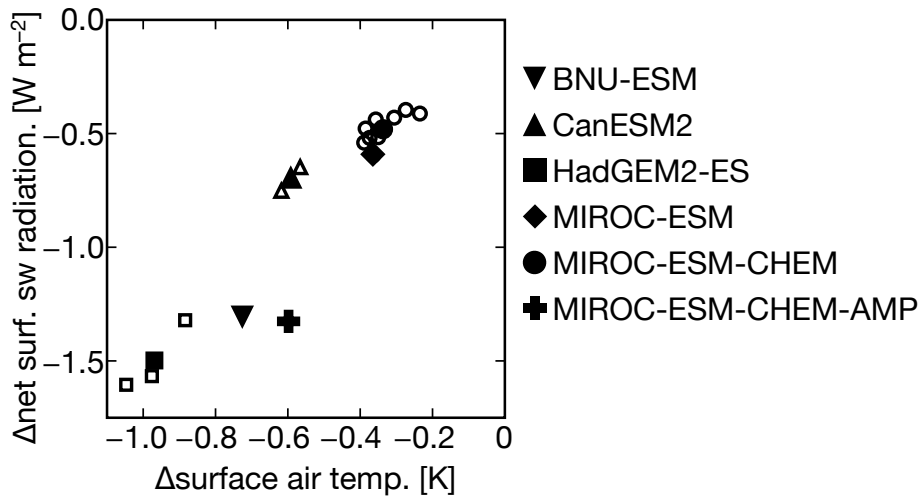
Figure 3. Relationship between the difference in the globally and temporally averaged surface air temperature (x-axis) and that of the net shortwave radiation at the surface (y-axis). The term of average is from 2040 to 2069. For CanESM2, HadGEM2-ES, and MIROC-ESM-CHEM, the ensemble mean is shown by filled symbols and the each member by unfilled ones.
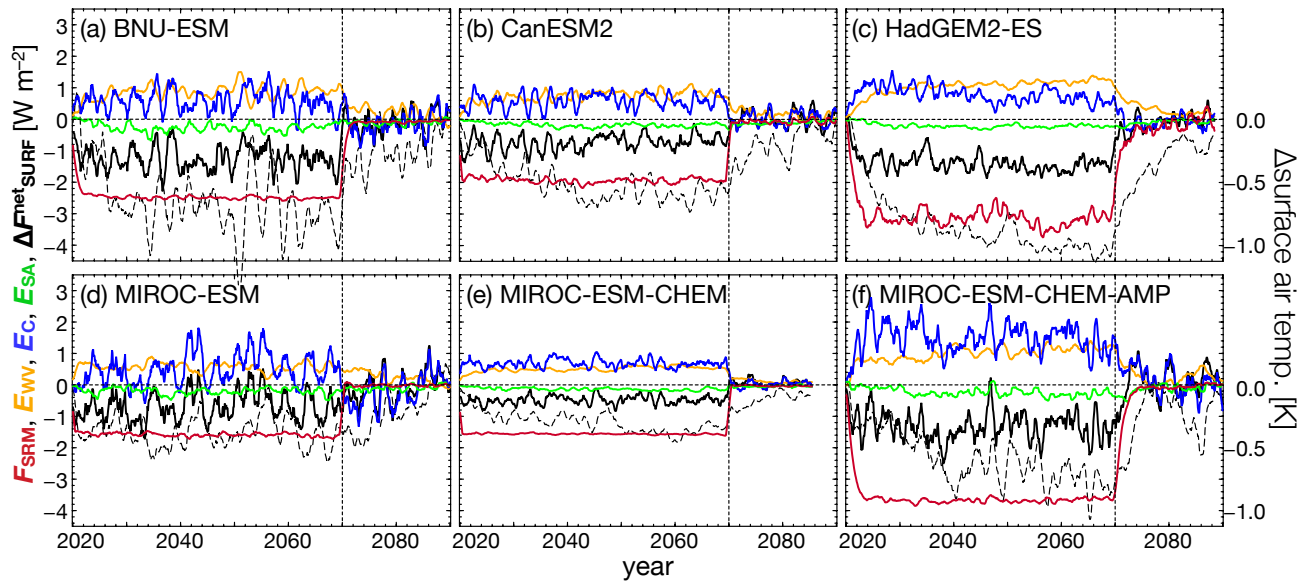
Figure 4. Same as Fig. 2 but for the SRM forcing (red), SW feedback due to changes in the water vapour (orange), cloud amounts (blue), and surface albedo (green) defined in Eqs. (9–12), and the difference in the net shortwave radiation at the surface (black, solid). The difference in the surface air temperature is also plotted by dashed-black curves whose values are shown by the right axis.
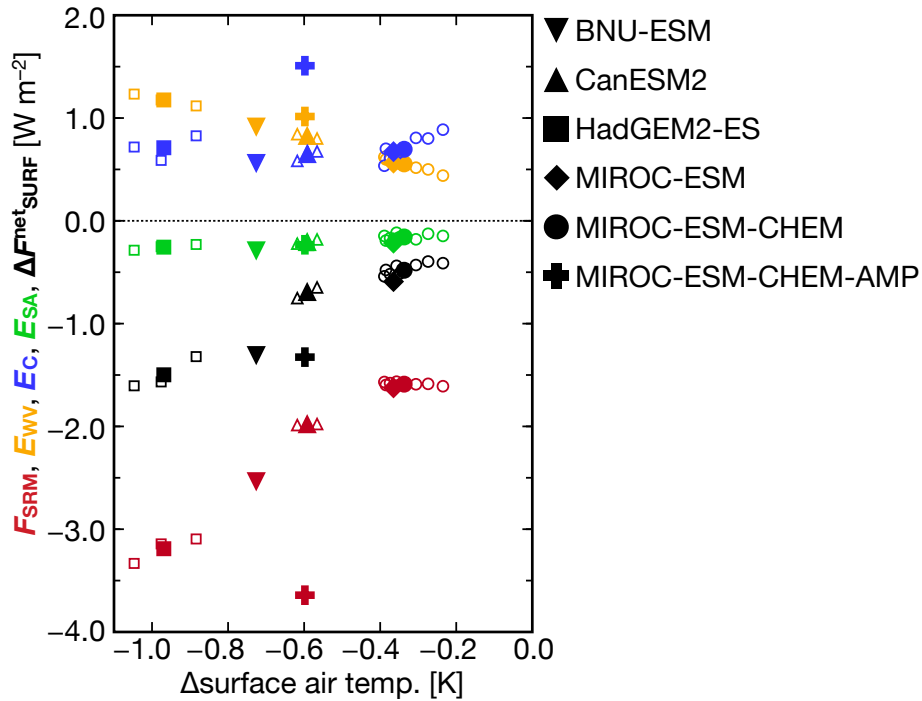
Figure 5. Same as Fig. 3 but also for SRM forcing (red), SW feedback due to changes in the water vapour amount (orange), cloud amount (blue), and surface albedo (green).
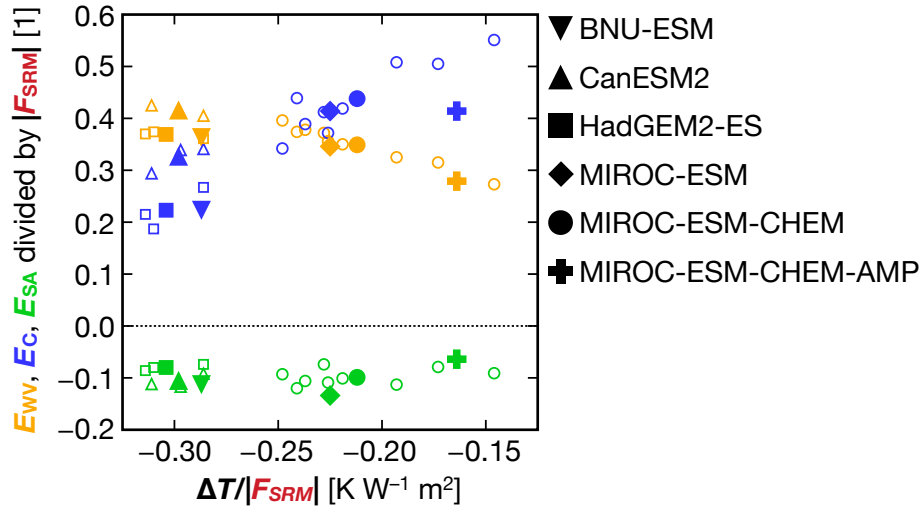
Figure 6. Same as Fig. 5 but for the SW feedback effects normalized by the absolute value of the SRM forcing. Note that the difference in the surface air temperature (x-axis) is also divided by $|F_{SRM}|$.
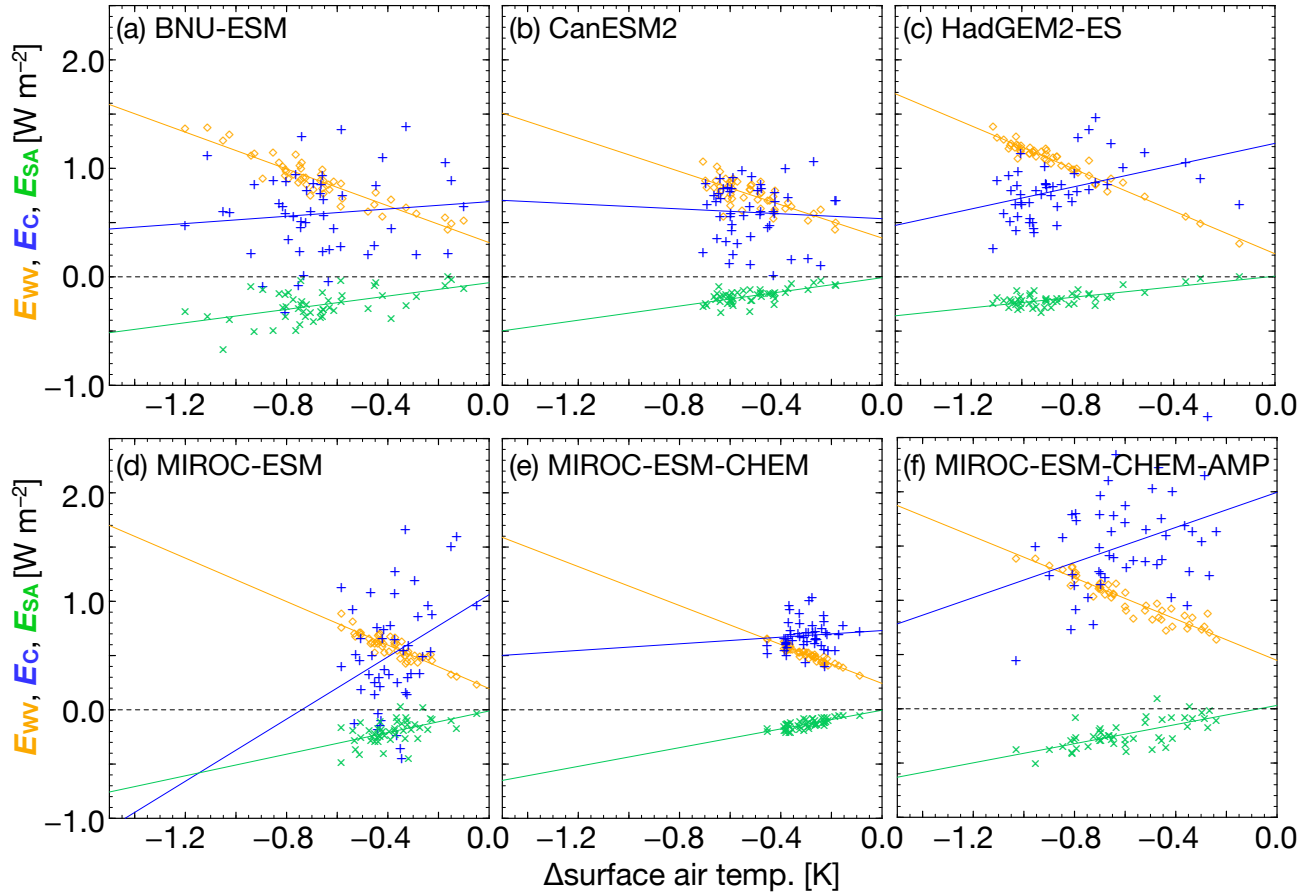
Figure 7. Globally and annually averaged relationship between ΔT (x-axis) and E_{WV} (orange $\diamond$), E_C (blue $+$), and E_{SA} (green $\times$) for each year. Regression line for each plot is shown by the same color, and a slope (feedback parameter), a y-intercept (rapid adjustment), and a correlation coefficient for each plot are shown in Table 2. Ensemble mean data are used for the plots on (b) CanESM2, (c) HadGEM2-ES, and (e) MIROC-ESM-CHEM.
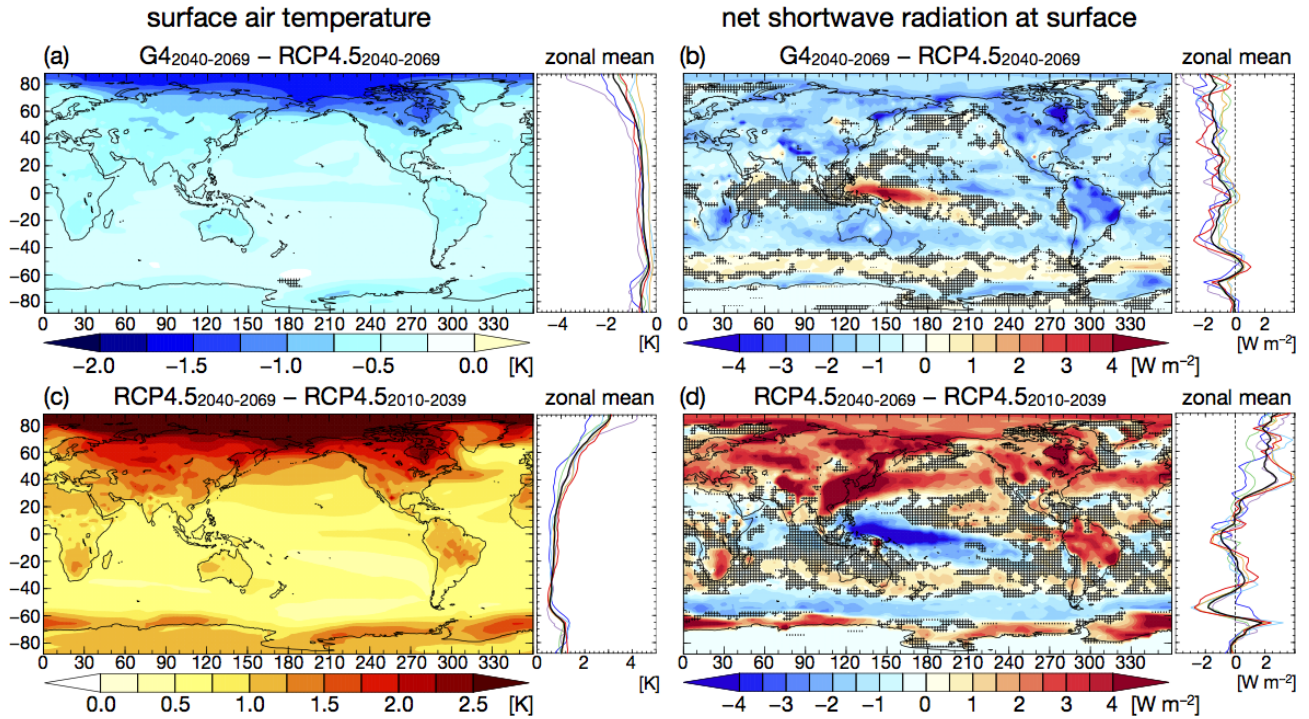
Figure 8. Multi-model mean of difference in the surface air temperature and net shortwave radiation at the surface. Panels (a) and (b) show the difference between G4 and RCP4.5 averaged over 2040–2069. Panels (c) and (d) show the difference between RCP4.5 averaged over 2040–2069 and that over 2010–2039. The colour shading shows the horizontal distribution of the multi-model mean and the black thick line on the right-hand side shows the zonal mean of the multi-model mean. Other coloured thin lines display the ensemble mean (or the result of the single run) of each model (blue: BNU-ESM, green: CanESM2, purple: HadGEM2-ES, cyan: MIROC-ESM, orange: MIROC-ESM-CHEM, red: MIROC-ESM-CHEM-AMP). Hatching indicates the region where 2 or more models (out of 6) disagreed on the sign of the difference.
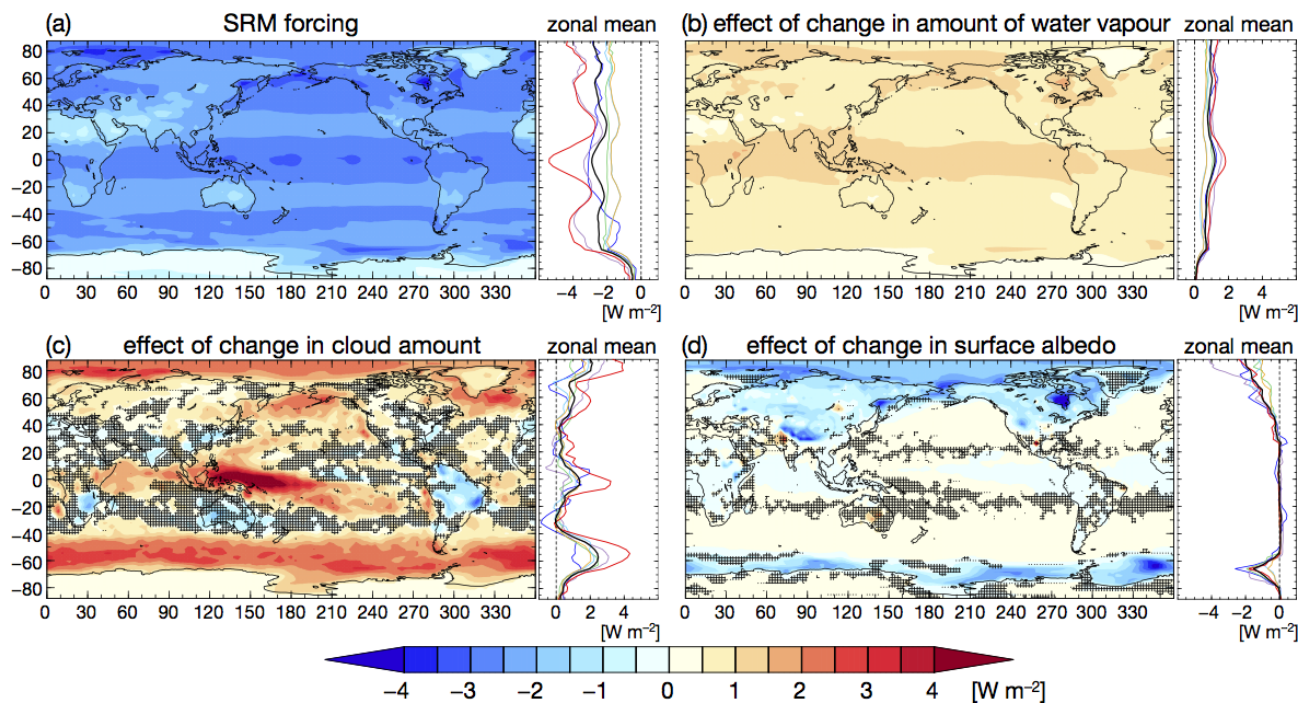
Figure 9. Same as Fig. 8 but for multi-model mean of (a) SRM forcing, SW feedback due to changes in the (b) water vapour amount, (c) cloud amount, and (d) surface albedo, averaged over 2040–2069.
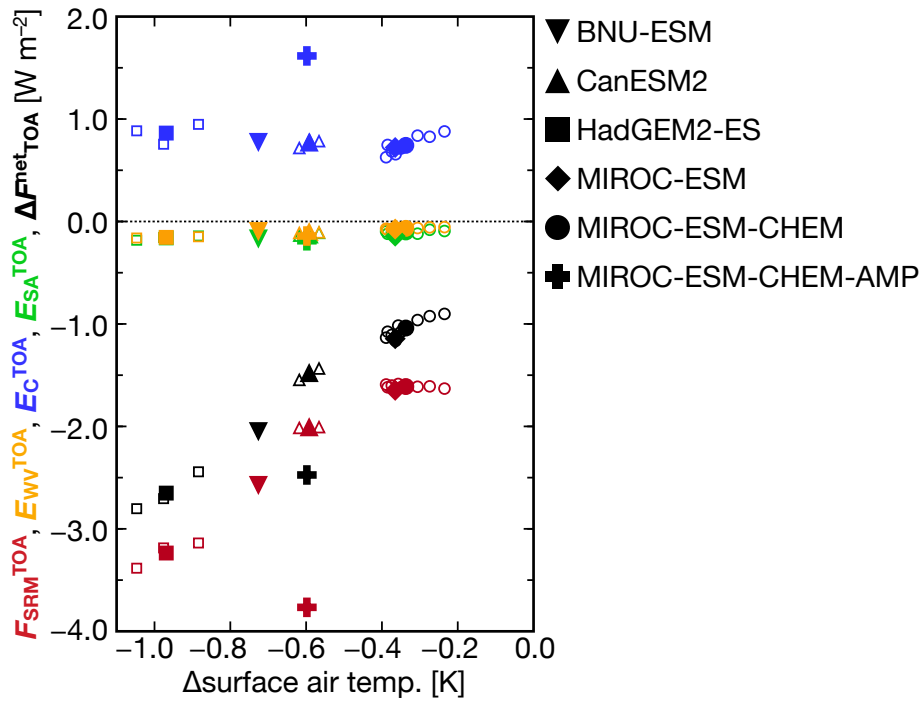
Figure 10. Same as Fig. 5 but the variables except for the surface temperature are calculated at the top of the atmosphere.
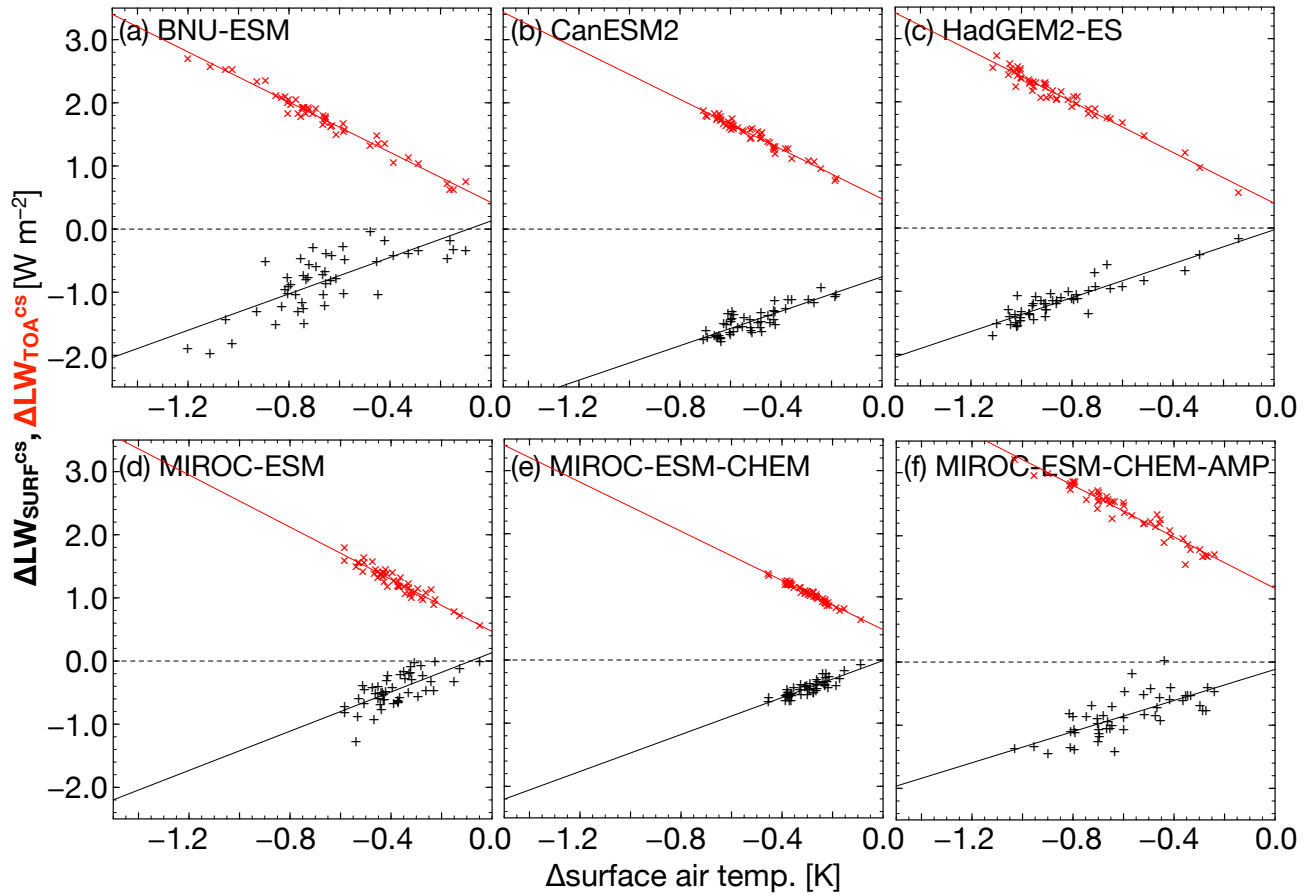
Figure 11. Same as Fig. 7 but for changes in net LW for clear-sky at the surface (black +) and that at TOA (red ×).

Table 1. Models participating in GeoMIP G4 experiments and used in this study. Manners of simulating sulphate aerosol optical depth (AOD), particle sizes and standard deviation of their log-normal distribution (σ), and ensemble members are shown for each model.

Models	sulphate AOD	Particle size [μm] (σ)	Ensemble Members
BNU-ESM Ji et al. (2014)	Prescribed	0.426 (1.25)	1
CanESM2 Arora and Boer (2010); Arora et al. (2011)	Uniform	0.350 (2.0)	3
HadGEM2-ES Collins et al. (2011)	Internally Calculated	0.0065 (1.3), 0.095 (1.4)	3
MIROC-ESM Watanabe et al. (2011)	Prescribed	0.243 (2.0)	1
MIROC-ESM-CHEM Watanabe et al. (2011)	Prescribed	0.243 (2.0)	9
MIROC-ESM-CHEM-AMP Watanabe et al. (2011); Sekiya et al. (2016)	Internally Calculated	0.243 (2.0)	1

Table 2. Values of rapid adjustment (Q_X) [Wm^{-2}], feedback parameter ($-P_X$) [Wm^{-2}K^{-1}], and correlation coefficient (R$_X$) due to changes in where X = WV, C, SA. Multi-model means are also shown.

Models	Q_{WV}	$-P_{\mathrm{WV}}$	R$_{\mathrm{WV}}$	Q_{C}	$-P_{\mathrm{C}}$	R$_{\mathrm{C}}$	Q_{SA}	$-P_{\mathrm{SA}}$	R$_{\mathrm{SA}}$
BNU-ESM	0.32	−0.85	−0.93	0.69	0.17	0.11	-5.4×10^{-2}	0.31	0.52
CanESM2	0.36	−0.77	−0.74	0.54	−0.11	−0.06	-7.9×10^{-3}	0.33	0.66
HadGEM2-ES	0.21	−0.99	−0.97	1.23	0.50	0.41	6.0×10^{-3}	0.24	0.71
MIROC-ESM	0.20	−1.00	−0.90	1.06	1.43	0.33	-1.1×10^{-2}	0.50	0.52
MIROC-ESM-CHEM	0.24	−0.90	−0.95	0.73	0.15	0.09	-3.5×10^{-3}	0.43	0.75
MIROC-ESM-CHEM-AMP	0.45	−0.95	−0.94	2.00	0.81	0.36	3.1×10^{-2}	0.44	0.68
Multi-model mean	0.30	−0.91	−0.91	1.04	0.49	0.21	-6.5×10^{-3}	0.38	0.64